Cell

Spatial organization and detection of social odors in mouse primary olfactory system

Graphical abstract

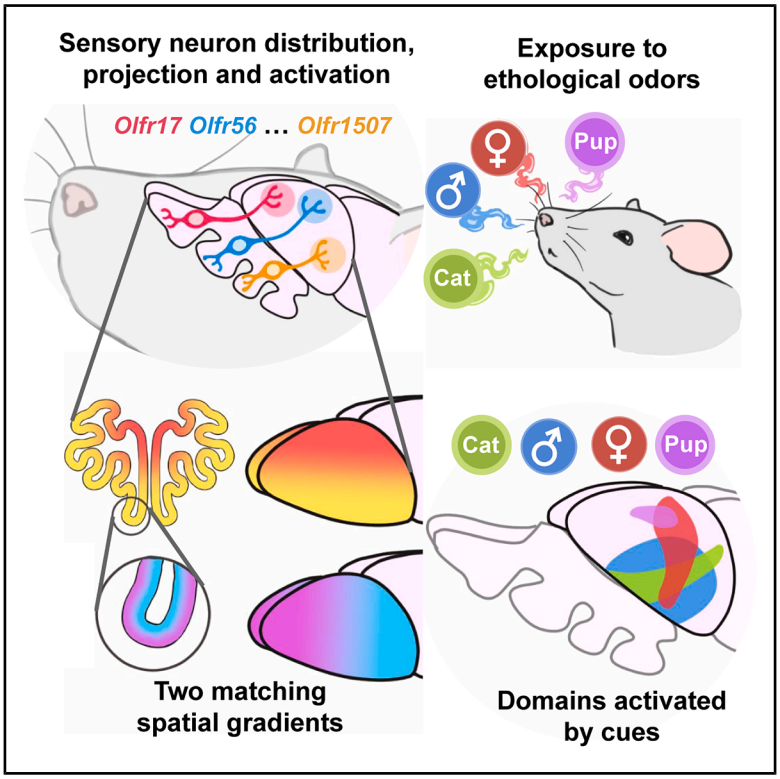

Authors

Bogdan Bintu, Yoh Isogai, Ignatius Jenie, Xiaowei Zhuang, Catherine Dulac

Correspondence

bbintu@health.ucsd.edu (B.B.), zhuang@chemistry.harvard.edu (X.Z.), dulac@fas.harvard.edu (C.D.)

In brief

Comprehensive atlases of olfactory sensory neuron distribution and axonal projection reveal a precise topographical organization and define spatial domains activated by social odors.

Highlights

- MERFISH captures the near-complete olfactory receptor expression in the MOE and OB
- Sensory neurons form two central-peripheral and apical-basal gradients in the MOE
- Olfactory bulb projections mirror epithelial gradients along two stereotypical axes
- Social and predator odors activate sensory neurons projecting to distinct spatial domains

Bintu et al., 2026, Cell *189*, 1–18
May 28, 2026
https://doi.org/10.1016/j.cell.2026.03.053

CellPress

Please cite this article in press as: Bintu et al., Spatial organization and detection of social odors in mouse primary olfactory system, Cell (2026), https://doi.org/10.1016/j.cell.2026.03.053

Cell

CellPress
OPEN ACCESS

Article

Spatial organization and detection of social odors in mouse primary olfactory system

Bogdan Bintu,[1,2,3,4,5,*] Yoh Isogai,[1,4,6] Ignatius Jenie,[5] Xiaowei Zhuang,[2,3,4,*] and Catherine Dulac[1,4,7,*]
[1]Department of Molecular and Cellular Biology, Howard Hughes Medical Institute, Harvard University, Cambridge, MA 02138, USA
[2]Department of Chemistry and Chemical Biology, Howard Hughes Medical Institute, Harvard University, Cambridge, MA 02138, USA
[3]Department of Physics, Howard Hughes Medical Institute, Harvard University, Cambridge, MA 02138, USA
[4]Center for Brain Science, Harvard University, Cambridge, MA 02138, USA
[5]Department of Cellular and Molecular Medicine, University of California, San Diego, San Diego, CA 92093, USA
[6]Allen Institute for Neural Dynamics, Seattle, WA 98109, USA
[7]Lead contact
*Correspondence: bbintu@health.ucsd.edu (B.B.), zhuang@chemistry.harvard.edu (X.Z.), dulac@fas.harvard.edu (C.D.)
https://doi.org/10.1016/j.cell.2026.03.053

SUMMARY

The detection of olfactory cues is essential to signal food, predators, and social encounters. To determine how the sensory detection of physiologically relevant odors is systematically mapped into the mouse primary olfactory system, we used multiplexed error-robust fluorescent *in situ* hybridization (MERFISH) to construct a molecular atlas of olfactory receptor (OR) expression in the main olfactory epithelium (MOE) and olfactory bulb (OB). We comprehensively quantified the expression of the mouse OR repertoire and uncovered stereotypical gradients of sensory neuron distribution in the MOE along two axes, central-to-peripheral and apical-to-basal. Projections of sensory neurons mirror these two MOE gradients along the dorsal-ventral and anterior-posterior axes of the OB, respectively. Integration with sequencing data revealed candidate signaling molecules underlying this spatial organization. Co-imaging OR and activity marker expression identified distinct spatial domains of sensory responses in the MOE and OB, providing a topographical basis for olfactory responses to ethologically relevant odors.

INTRODUCTION

The mammalian main olfactory epithelium (MOE) detects a vast range of environmental cues to signal the presence of food, predators, and conspecifics.[1,2] Within the rodent MOE, odor cues are detected by olfactory sensory neurons (OSNs), which each express a single olfactory receptor (OR) gene out of a large ~1,000 *OR* gene family through an intricate mode of transcriptional regulation.[3–8] Expression of specific axonal guidance and signaling molecules enables OSNs with a given *OR* to project into distinct pairs of glomeruli at stereotyped positions of the olfactory bulb (OB), generating an organized map of odor sensing.[9–11]

Previous studies have partially characterized the spatial organization of OSNs within the MOE and their projections to the OB. In the MOE, expression of individual *ORs* was restricted within concentric olfactory zones, whose position is highly stereotypical across individuals in a given species.[12,13] Initially identified as 4–5 discrete olfactory zones,[12,13] additional *in situ OR* measurements uncovered other, partially overlapping, olfactory zones.[14,15] In turn, initial spatial transcriptomics approaches provided a more comprehensive, yet so far low spatial resolution view of *OR* organization[16,17] and suggested a continuous, rather than discrete spatial distribution of *ORs* along the central-peripheral axis of the MOE.

Within the OB, specific *OR* transcripts are localized to sensory axon terminals in stereotyped, bilaterally symmetric pairs of glomeruli—one medial and one lateral—per hemisphere.[9,10] Transgenic labeling strategies[11,18,19] and newly developed spatial transcriptomics approaches[20,21] enabled mapping of OR projections, although these efforts remain incomplete, with only a fraction of the *OR* repertoire mapped to the OB to date.

The stereotypy of OSN projections has suggested the presence of a chemotopic map of OR activation in the OB.[1,2,9,10,22] Functional imaging of the dorsal OB in animals exposed to chemical compounds indeed revealed activation of distinct topographical domains within the OB.[23–28] However, further progress in connecting the spatial organization and OB projection of OSNs with their sensory function is impeded by the lack of complete molecular atlases of *OR* expression in the MOE and OB and the lack of functional annotations of each OR response to physiologically relevant cues. Numerous methods developed to catalog OR responses to different olfactory cues,[29] including recent high-throughput *in vivo* screens,[30–33] have used unnaturally high concentrations (mM range) of single compounds and have yet to comprehensively describe the OR responses to naturalistic and physiologically relevant odors involved in animal behavior.

Please cite this article in press as: Bintu et al., Spatial organization and detection of social odors in mouse primary olfactory system, Cell (2026), https://doi.org/10.1016/j.cell.2026.03.053

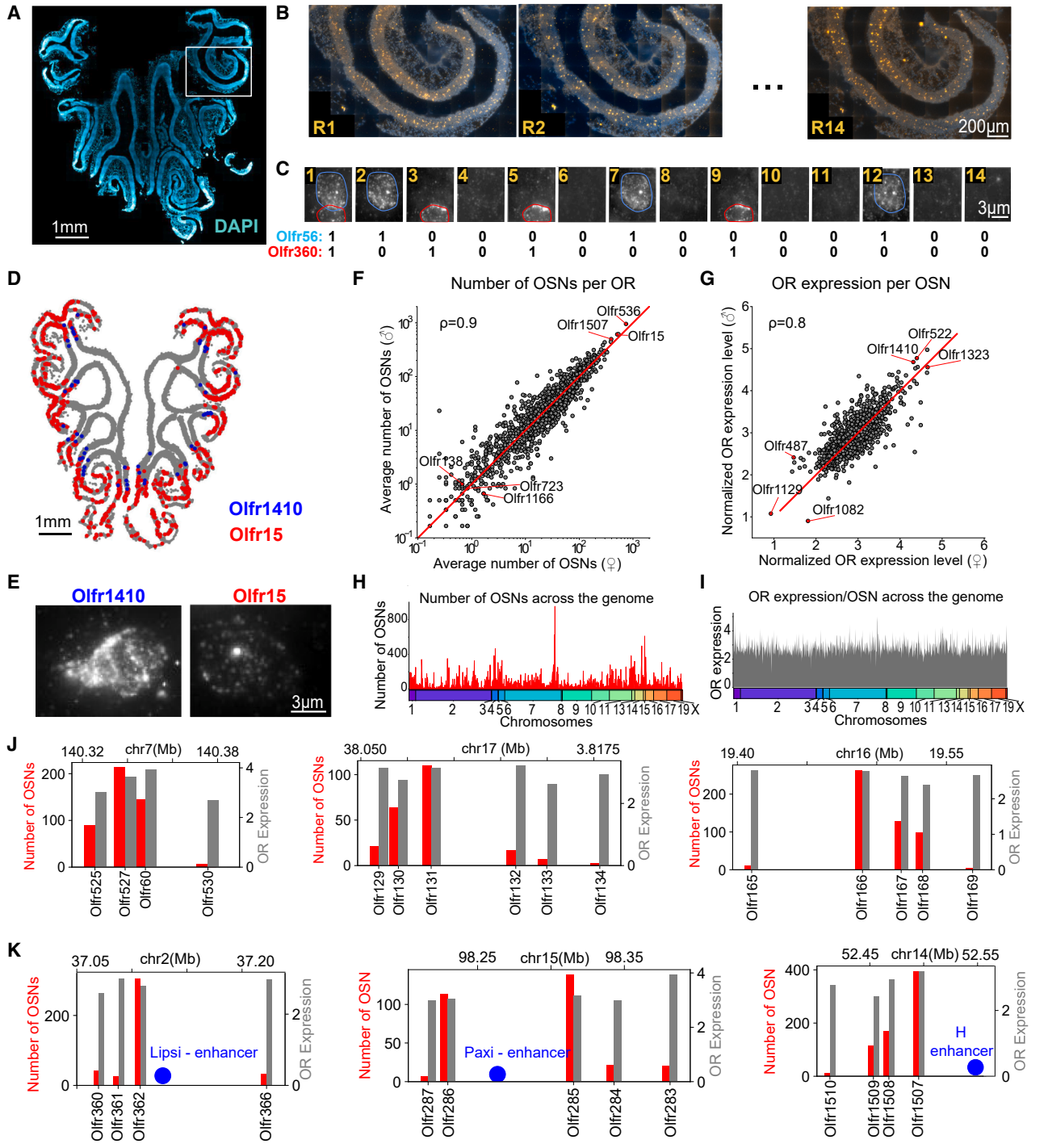

Figure 1. MERFISH-based high-throughput imaging of the OR repertoire

(A) Coronal section of the MOE (16 μm) hybridized with MERFISH probes for 200 *ORs*. DAPI staining in blue.

(B) Subregion from (A) showing MERFISH readout signals (yellow).

(C) 14-cycle MERFISH signal identifying *Olfr56* and *Olfr360* OSNs based on unique binary barcodes.

(D and E) Spatial distribution (D) and representative high-magnification MERFISH images (E) of *Olfr1410* (blue) or *Olfr15* (red) OSNs.

(F and G) Correlation between male and female animals of the average OSN count per section for each OR (F) and the average OR expression per cell (G). Expression level was estimated from the brightness of the MERFISH signal and normalized by the average brightness across the MOE.

(legend continued on next page)

Please cite this article in press as: Bintu et al., Spatial organization and detection of social odors in mouse primary olfactory system, Cell (2026), https://doi.org/10.1016/j.cell.2026.03.053

In this study, we leveraged the sensitivity of the spatial transcriptomics method multiplexed error-robust fluorescent *in situ* hybridization (MERFISH)[34] to assess the expression of the near-complete repertoire of ~1,100 *ORs* and ~10 *TAARs* within the MOE and the OB. By further combining MERFISH with single-molecule fluorescence *in situ* hybridization (FISH) for *Egr1*, a marker of neuronal activity in chemosensory organs,[35,36] we characterized the OR responses to ethologically relevant social odors. The integration of the spatial organization of *ORs* with their functional characteristics uncovered the existence of spatial domains responding to distinct physiologically relevant olfactory signals.

RESULTS

In situ mapping of the near-complete repertoire of odorant receptor gene expression in the MOE using MERFISH

MERFISH is a single-cell transcriptome imaging approach that quantifies expression of thousands of genes in individual cells within tissues.[34,37–39] To detect the near-complete repertoire of *ORs*/*TAARs*, we implemented two key modifications[37]: First, to overcome the high sequence similarity between the coding sequences of receptor genes, probes (Table S1) were preferentially designed against a refined map[40] of the divergent untranslated regions (UTRs) (Figures S1A and S1B). Second, to increase detection sensitivity, we combined split probes[41] and multiplexed branched DNA amplification[42] (Figure S1C).

We imaged MOEs from 13 mice (8 males and 5 females) across six coronal positions spanning ~1.5 mm along the anterior-posterior (A-P) axis (Figures S2A and S2B). For each A-P position, 2–5 consecutive 16-μm sections were imaged by MERFISH, with a distinct set of 200–500 *ORs* assessed per section (Figures 1A–1C). Sections were registered to reconstruct the near-complete *OR*/*TAAR* expression atlas at each A-P position.

To validate the *OR* identification, we used two transgenic lines, Olfr17-IRES-tau-lacZ[11] (N = 1) and Olfr16-IRES-tau-GFP[43] (N = 1), in which OSNs co-expressed *Olfr17* and beta-galactosidase (*β-gal*), or *Olfr16* and green fluorescent protein (*GFP*). Across two sections per animal, MERFISH captured 75%–77% of reporter-positive cells with a specificity of 95%–98%, defined as the percent of Olfr17/Olfr16-positive cells expressing the corresponding reporter (Figures S1D–S1I). These results indicate the high sensitivity and accuracy of our experimental paradigm to quantify the *OR* identity of OSNs by MERFISH.

Representation and expression levels of ORs in the MOE

Using MERFISH, we quantified the average number of OSNs per section expressing a given *OR* and the average expression level of each *OR* per cell (Figures 1D–1G, S2C, and S2D; Table S2). The abundance of OSN types and per-cell receptor expression levels were similar between males and females (Pearson's correlation coefficients of 0.9 and 0.8, respectively; Figures 1F and 1G) and consistent with reports from bulk RNA sequencing (RNA-seq).[40] MERFISH quantifications correlated with data from single-cell RNA sequencing (scRNA-seq)[44] (Figure S2E) and bulk RNA-seq across ~35% of the MOE along the AP axis (Figures S2F and S2G). This suggests an accurate estimation of OSN population sizes and OR expression levels within the anterior-central region of the MOE sampled.

A three-order-of-magnitude variation in OSN population sizes was found across the OR repertoire (Figure 1F). The most abundant *ORs* (including *Olfr536*, *Olfr15*, and *Olfr1507*) were expressed in >350 OSNs per section, while 5.2% of receptors (including *Olfr1166*, *Olfr138*, or *Olfr723*) were detected in <1 OSN per section. By contrast, per-cell expression levels were relatively uniform, generally varying by less than an order of magnitude (Figure 1G).

To determine whether genomic context is associated with OSN population size, we mapped OSN abundances against genomic coordinates. Population sizes were non-uniform across the genome, forming genomic peaks and valleys. Specifically, OSN abundance progressively decreased with the genomic distance from the most abundant 100 ORs (Figures 1H–1J, S2H, and S2I). By contrast, per-cell expression levels were less variable across the genome (Figures 1H–1J, S2J, and S2K) and only weakly correlated with OSN population sizes (Pearson's correlation coefficient of 0.1). Notably, ORs located near known super-enhancers (i.e., *H-element* or *Greek islands enhancers*)[45] (Figures 1K and S2L–S2O) were expressed by higher numbers of OSNs, consistent with an enhancer-based regulation of OR choice.

Spatial organization of the OR repertoire within the MOE

OSN types have distinct localization patterns within the MOE (Figure 2A). To systematically quantify OSN's spatial distributions, we calculated the spatial overlap for each pair of *ORs* (defined as the fraction of OSNs of the corresponding *ORs* within 200 μm) across all 13 animals imaged. The uniform manifold approximation and projection (UMAP) embedding of the spatial overlap placed the *ORs* along a thin, curved coordinate (Figure 2B; Table S3). OSN types overlapped with multiple adjacent types along this UMAP coordinate in a graded fashion (Figure 2C), suggesting a continuous OSN distribution in the MOE. We observed a slight enrichment in the spatial overlap of a group of ~400 *ORs* (Figure 2C, top left), which corresponds to the Class I receptors and includes nearly all previously annotated zone 1 *ORs*.[16]

Visualizing OSNs colored according to their UMAP coordinate within the MOE sections revealed that most OSNs form overlapping rings that continuously expand from the center to the periphery (Figure 2D). This organization was highly stereotypical across animals (Figures 2E and 2F). While each *OR* was expressed primarily within a ring-like zone, consistent with prior reports,[14] our comprehensive mapping further revealed that the

(H and I) OSN type abundance (H) and OR expression level per OSN (I) plotted by the genomic coordinates. Chromosomal labels are indicated by a colorbar.
(J) Bar plots of OSN abundance (red) and per-OSN OR expression (gray) for representative OR genomic clusters.
(K) Same as (J) for OR genomic clusters close to known enhancers (blue).
See also Figures S1 and S2.

Please cite this article in press as: Bintu et al., Spatial organization and detection of social odors in mouse primary olfactory system, Cell (2026), https://doi.org/10.1016/j.cell.2026.03.053

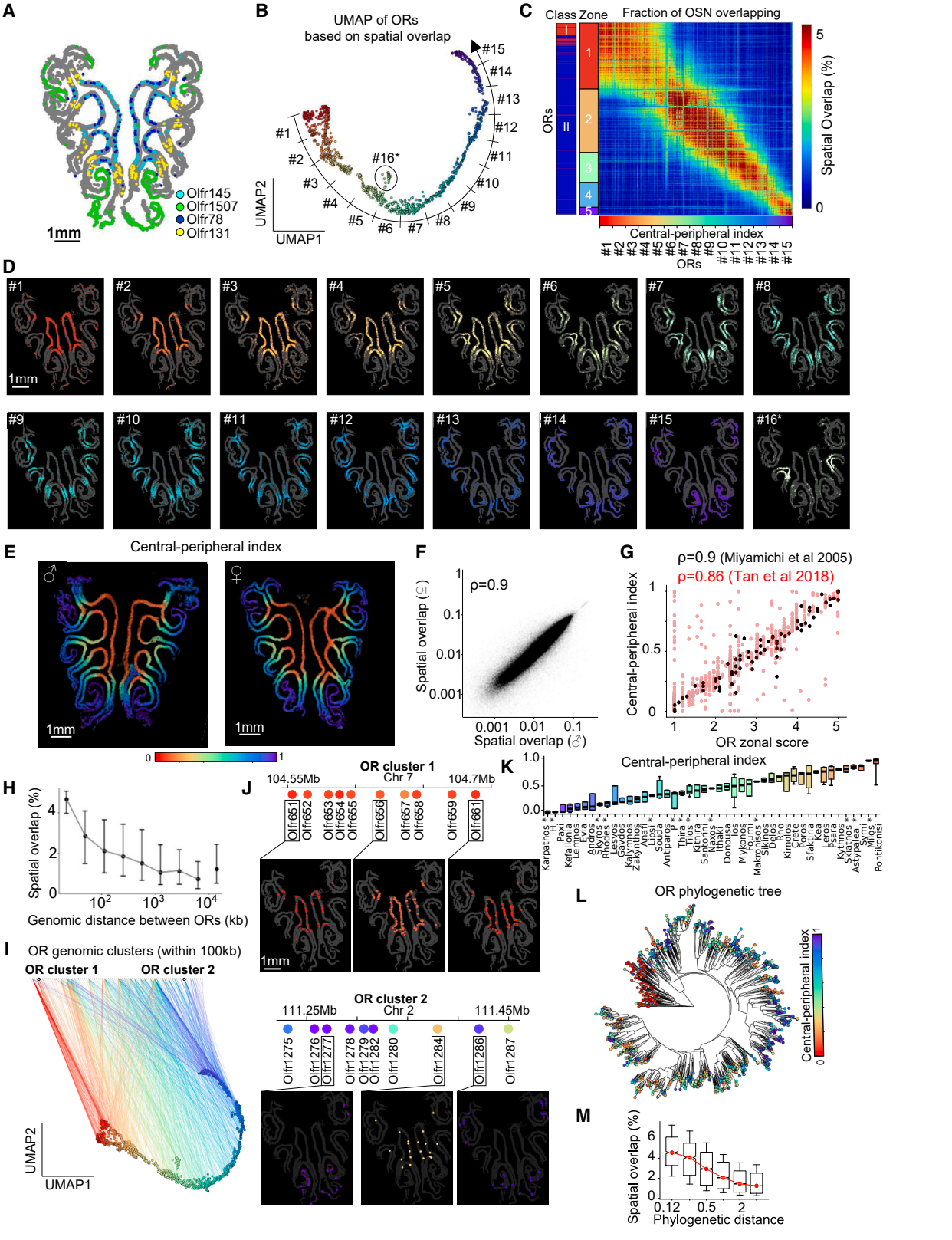

(legend on next page)

Please cite this article in press as: Bintu et al., Spatial organization and detection of social odors in mouse primary olfactory system, Cell (2026), https://doi.org/10.1016/j.cell.2026.03.053

positions of these rings changed in a continuous fashion across ORs, impeding the definition of precise zonal boundaries (Figures 2E and 2F). Noticeable exceptions included a small group of ORs, previously associated with "the unusual zone" of the MOE,[46] that separated from the UMAP coordinate and were constrained to a specific mid-region of the MOE (Figures 2B and 2D, marked as #16*). Additionally, *TAARs*, which did not form a continuous distribution along the entire MOE, were expressed either within the central or a mid-peripheral ring of the MOE (Figures S3A and S3B).

Validating these results, a close correspondence was observed between the central-peripheral distribution of *ORs* quantified by MERFISH and the prior zonal annotations either measured by *in situ* hybridization for ~80 *ORs*[15] (Figure 2G, black dots) (Pearson's correlation of 0.9) or computationally inferred by a sequencing-based approach[16] (Figure 2G, red dots).

We next explored potential factors underlying the OR spatial organization, including genome location and sequence similarity.[31] *ORs* in close genomic proximity had higher spatial overlap than genomically distal *ORs* (Figure 2H). Accordingly, *ORs* within the same genomic cluster tended to be expressed within the same ring-like structure in the MOE (Figures 2I–2K). For instance, the *ORs* in cluster *Olfr651-Olfr661* were all expressed within the central ring of the MOE. Similarly, most *ORs* in cluster *Olfr1275-Olfr1287* were expressed in the same peripheral MOE ring, with a few exceptions (i.e., *Olfr1284* and *Olfr1287*) (Figure 2J). *ORs* close to previously annotated enhancers had a largely overlapping spatial distribution, supporting an enhancer-mediated coordination of spatial expression (Figure 2K).

Phylogenetic analysis further showed that *ORs* with high sequence similarity had higher spatial overlap (Figures 2L and 2M). To estimate the relative contributions of genomic distance and phylogenetic similarity to the spatial overlap of the corresponding OSNs, we fitted a multivariate linear regression model (see STAR Methods). Genomic distance and phylogenetic similarity predicted comparable portions of the variance in spatial overlap (R^2 = 0.043 and 0.048, respectively). When combined, the predicted variance increases to 0.056, supporting a contribution from both factors to the OR spatial distribution. We note, however, that disambiguating the contributions of genomic distance and phylogenetic similarity is difficult because these measures are highly correlated (with a Pearson's correlation of 0.56), likely due to tandem duplications of ORs during evolution.[47] Nonetheless, these results are consistent with a model in which spatially patterned transcription factors[48] recruited to similar sequences in the OR gene body and/or shared neighboring regulatory sequences enable ORs to be coregulated spatially. Further mapping of transcription factor binding sites and enhancer-promoter interactions[5,45,48] may help establish a comprehensive model of how OR expression is spatially regulated.

Mapping the projections of olfactory sensory neurons to the OB

We leveraged the high sensitivity of MERFISH to systematically track *OR* transcripts in OSN axon terminals within OB glomeruli. MERFISH was performed on serially sectioned bilateral OBs from 2 adult females (Figure 3A). Glomeruli were segmented in each section using neural network-based models[49] applied to images of nuclear-stained periglomerular cells. OR identity was assigned to glomeruli based on dominant *OR* expression (threshold > 10 *OR* transcripts), uncovering 1–3 glomeruli per *OR* per hemi-bulb (Figures 3B and 3C). 3D reconstruction from registered serial sections yielded an OB projection map across 641 receptors (Figures 3D and S3C).

To validate the accuracy of the projection map, we selected 5 *ORs* (*Olfr15*, *Olfr16*, *Olfr17*, *Olfr155*, and *Olfr1507*) whose 3D projections were previously determined using transgenic reporters[18] (Figure S3D). The comparison of pairwise distances between the OB projections of these ORs in our MERFISH dataset and the published report demonstrated a tight correspondence (Figures S3D–S3F) (Pearson's correlation of 0.94).

The OB projections from left and right hemispheres showed a striking mirror-symmetry across both medial and lateral projections (Figures 3E and 3F). Quantitatively, the registered 3D positions between left and right OBs aligned within ~250 μm

Figure 2. Spatial organization of OSNs in the MOE

(A) Coronal MOE section (gray) highlighting the spatial distribution of four example OSN types: *Olfr145*, *Olfr1507*, *Olfr78*, *Olfr131*.

(B) UMAP embedding of OSN types based on pairwise spatial overlap. *ORs* are colored by their position along the emerging UMAP curved trajectory (central-peripheral index, 0–1) and divided into 16 groups (#1–#16).

(C) Matrix of pairwise spatial overlap (fraction of pairs of OSNs within 200 μm for each *OR* pair) across *ORs*, sorted by the central-peripheral index. Annotations indicate OR class and zonal information.[15,16]

(D) Image series of an MOE section onto which groups of ~70 *ORs* progressively covering the UMAP coordinate in (B) are shown. Group #16* covers the unusual zone *ORs*.

(E) Representative MOE sections from male and female animals with OSNs colored by the central-peripheral index.

(F) Correlation between spatial overlap of OSNs across sexes.

(G) Correlation between the MERFISH central-peripheral index and the zonal scores previously published.[15,16]

(H) Correlation between spatial overlap and genomic distance of *ORs*. The terminal disconnected point marks intrachromosomal OR pairs. Dots mark means, and error bars mark the standard error of the mean.

(I) Linkage map connecting UMAP coordinates (B) to genomic *OR* clusters (containing *ORs* within 100-kb).

(J) Spatial distribution of OSNs across two representative *OR* genomic clusters.

(K) Box plots of central-peripheral index for *ORs* within 100kb of previously annotated enhancers. Asterisks denote enhancers if neighboring *ORs* have lower variance than expected by chance ($p < 0.05$).

(L) Phylogenetic tree of *ORs*[31] colored by the central-peripheral index.

(M) Correlation between OR phylogenetic distance and spatial overlap. Box plots indicate 25th/75th percentiles; notches denote 95% confidence intervals; whiskers mark the 15th/85th percentiles.

See also Figure S3.

Please cite this article in press as: Bintu et al., Spatial organization and detection of social odors in mouse primary olfactory system, Cell (2026), https://doi.org/10.1016/j.cell.2026.03.053

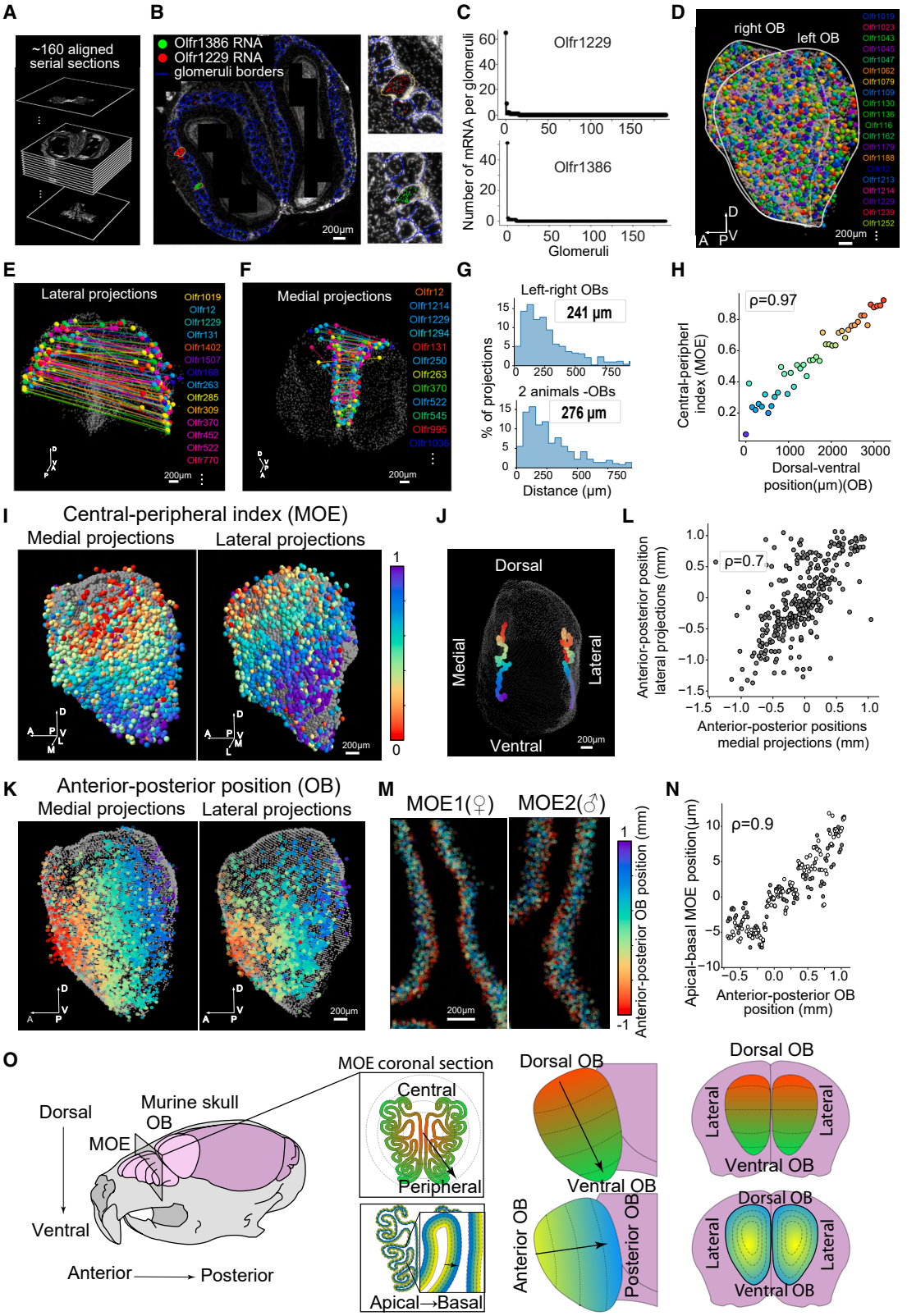

(legend on next page)

Please cite this article in press as: Bintu et al., Spatial organization and detection of social odors in mouse primary olfactory system, Cell (2026), https://doi.org/10.1016/j.cell.2026.03.053

(Figure 3G, top). Similarly, across different animals, projections aligned within a median distance of 276 μm (Figure 3G, bottom), indicating that OR projections are spatially specified within an accuracy of ~3 glomeruli diameters across the OR repertoire. Leveraging this stereotypy, a consensus projection map was constructed by aligning the four imaged OBs into a common reference. This alignment enabled a more relaxed OR identification criterion, permitting glomeruli with >5 transcripts to be assigned to an OR if the same OR identities were observed in a similar position across multiple OBs (<500 μm). This approach increased the coverage to approximately 75% of the *OR* repertoire (Table S4).

Spatial organization of OSNs in the MOE versus projections to the OB

We next explored the spatial relationship between the distributions of OSNs in the MOE and their projections into the OB. Mapping OB projections by their central-peripheral position in the MOE (from Figures 2B, 2D, and 2E) revealed that continuous rings in the MOE mapped to continuous bands in the OB along the dorsal-ventral (D-V) direction in a highly correlated manner (Figures 3H–3J). The 3D position of projections, averaged along a sliding window of ~80 *ORs* sorted by central-peripheral MOE preference, formed two parallel D-V axes in both medial and lateral OB (Figures 3I and 3J). These results suggest that the central-peripheral preference of OSNs in the MOE is transferred to a D-V preference of projections into the OB, with symmetry across the medial and lateral sides of the OB.

We further examined the orthogonal A-P axis of the OB. As with the D-V axis, A-P projections were mirrored between medial and lateral glomeruli (Figures 3K and 3L) (Pearson's correlation of 0.8). Unexpectedly, mapping this A-P distribution of OB projections back to the MOE revealed an apical-to-basal gradient of OSN distribution in the neuroepithelium (Figures 3M and 3N; Table S5). Specifically, OSNs with anterior OB projections (i.e., *Olfr1170* and *Olfr1388*) were located consistently closer to the lumen (apical in MOE neuroepithelium), whereas OSNs with posterior OB projections (i.e., *Olfr354* and *Olfr99*) were located closer to the basal lamina (basal in MOE neuroepithelium) (Figures S4A–S4L). Finally, similarly to the MOE spatial distribution, ORs more similar in sequence were associated with closer OB projections along both the D-V and A-P axes of the OB (Figures S5A–S5D).

Consistent with our results, a subgroup of OSNs, corresponding to 71 *ORs*, that co-express *Cd36*/*Cd55* were previously found to be enriched in the apical region of the MOE and to project to the most anterior part of the OB.[50] Our MERFISH data recapitulated this finding (Figures S5E–S5I), and expanded it to establish a broad relationship between the apical-basal spatial distribution of OSNs in the MOE and their A-P projection in the OB across the entire *OR* repertoire.

Altogether, our data uncovered two sets of preferential axes governing olfactory topography (Figure 3O). In the MOE, OSNs form gradients along a larger-scale central-peripheral axis and a smaller-scale apical-basal axis. These two gradients of OSNs in the MOE were mirrored to two corresponding axes (D-V and A-P) of OB projections, in which the OSNs with a more central or apical preference in the MOE projected to the more dorsal or anterior regions of the OB, respectively.

Differential gene expression in OSNs according to OR spatial distribution in the MOE and OB

The spatial organization and projection of OSNs result from the coordinated expression of multiple genes encoding axonal guidance molecules, transcription factors, and other signaling molecules.[1,44] To correlate differential gene expression in OSNs with their spatial distribution and projections, we integrated published scRNA-seq data from adult OSNs[44] with MOE and OB spatial maps generated by MERFISH (Figure 4A). Specifically across the top ~5,000 differentially expressed genes (excluding *ORs*), the average scRNA-seq expression of each gene in each OSN type was imputed onto its MOE locations or onto its OB projections mapped by MERFISH (Figures 4A and 4B; STAR Methods). This imputation approach was validated by recapitulating known expression patterns, such as the complementary central-peripheral and D-V expression of *Ncam2* and *Nqo1* in the MOE and OB[51] (Figure 4B).

UMAP embedding (Figure 4C) of these spatial imputations revealed two primary continuous branches of expression: the top branch included genes such as *Adgrv1*, *Acsm4*, and *Rnd2*, for

Figure 3. 3D projections of OSNs into the OB

(A) Serial MERFISH imaging of ~160 coronal sections (16–18 μm) reconstructed into a 3D bilateral OB stack using DAPI-based alignment.
(B) Representative OB section marking transcripts identified for *Olfr1386* (green) and *Olfr1229* (red), in segmented glomeruli (blue). Glomeruli enriched in each OR are enlarged on the right. Image is composed of aligned high-resolution tiles.
(C) Distribution of *Olfr1386* (top) and *Olfr1229* (bottom) transcripts across glomeruli from the OB section in (B).
(D) 3D projection map with MERFISH-identified glomeruli colored by OR.
(E and F) Mirror-symmetry of lateral (E) and medial (F) projections between left and right OBs. Lines connect matching OR identities.
(G) Histograms of distances between matching OR projections across aligned bilateral OBs (top) or aligned OBs of different animals (bottom). Median distances are indicated.
(H) Correlation between the MOE central-peripheral index and the OB D-V position of projections. OB projections were binned in 150 μm intervals along the D-V axis.
(I) Consensus 3D projection map from four aligned OBs, colored by MOE central-peripheral index.
(J) The average position of OB projections across a sliding window (~80 ORs/window) across ORs sorted by MOE central-peripheral index.
(K) Left: medial OB projections colored by A-P position. Right: lateral OB projections colored by medial A-P position.
(L) Correlation of the A-P positions of medial versus lateral projections.
(M) Representative MOE sections with OSNs colored by the A-P position of their corresponding OB projections.
(N) Correlation between the average OB A-P projection position and the average MOE apical-basal position in male (gray) and female (white) mice.
(O) Schematic summarizing the two sets of matching axes of organization of OSNs in the MOE and their projections in the OB.
See also Figure S4.

Please cite this article in press as: Bintu et al., Spatial organization and detection of social odors in mouse primary olfactory system, Cell (2026), https://doi.org/10.1016/j.cell.2026.03.053

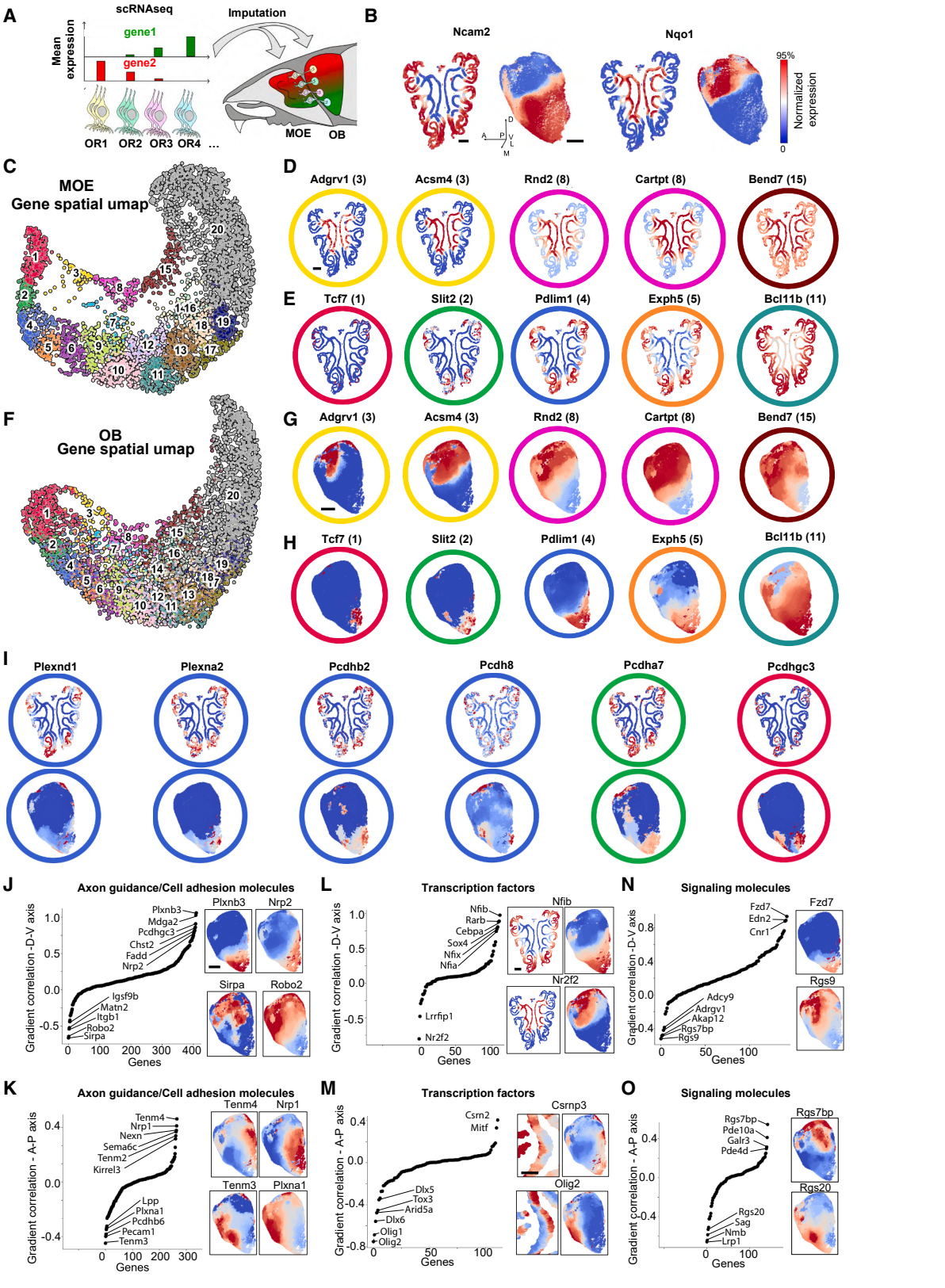

(legend on next page)

Please cite this article in press as: Bintu et al., Spatial organization and detection of social odors in mouse primary olfactory system, Cell (2026), https://doi.org/10.1016/j.cell.2026.03.053

which expression progressively expanded from the center to the periphery of the MOE (Figure 4D); the bottom branch included genes such as *Tcf7*, *Slit2*, and *Pdlim1*, which showed the opposite trend, with expression progressively expanding from the periphery toward the center (Figure 4E). The two opposing gradients of genes, which include many transcription factors, may help establish graded OR expression along the central-peripheral axis of the MOE. A similar UMAP topography was observed for gene imputations into the OB (Figures 4F–4H), consistent with the close correlation between the spatial distribution of OSNs and their OB projection (Figure 3). A subset of genes, including plexins and protocadherins, exhibited a different organization from this general trend. Despite being constrained to similar MOE regions, these genes formed discrete, partially overlapping patches in the OB (Figure 4I). These results may reflect a subset of genes associated with the local refinement of OSN projections in the OB, as previously proposed for the protocadherin gene family.[52]

Gene Ontology annotations[53] were used to classify differentially expressed genes, and three functional classes were further examined: axonal guidance/cell adhesion molecules, transcription factors, and signaling molecules. All three classes covered the entire UMAP spaces for both the MOE and OB (Figures S6A–S6E) and the expression profile of each class of genes was sufficient to predict the location of the OB projection with a median resolution of ~500 μm (see STAR Methods; Figures S6F–S6H), significantly more accurate than upon randomly shuffling the OSN identities (Wilcoxon test, p value < 0.001). These results support the model in which all three classes of genes cooperatively control OR specification, spatial distribution, and OB projection of OSNs.[54]

Genes were ranked based on the strength of their imputed gradient along the D-V and A-P axes of OB projection (Figures 4J–4O). The imputed OB gradients mirrored the imputed gradients in the MOE along the matching axes (Figures S6D and S6E). Among axonal guidance/cell adhesion molecules (Figures 4J and 4K), this analysis highlighted many previously established regulators of murine OB projections, including *Nrp1*, *Robo2*, *Plxna1*, or protocadherins,[52,55–57] as well as regulators of OB projections established in other species, including, for instance, teneurins in *Drosophila melanogaster* (Tenm2, Tenm3, and Tenm4).[58] Among transcription factors (Figures 4L–4O), this analysis highlighted *Nfia*, *Nfib*, and *Nfix*, shown to regulate zonal organization of ORs in the MOE,[48] and members of the retinoic acid pathway (i.e., *Rarb*) or the thyroid hormone pathway (i.e., *Nr2f2*), which remain to be further assessed. Among signaling molecules, we identified members of the G protein-coupled receptor signaling pathway (such as *Rgs7bp*, *Rgs9*, and *Rgs20*) and cyclic AMP signaling (such as *Pde10a* and *Pde4d*), supporting the proposed role of *OR* G-coupled signaling in defining axonal projection into the OB.[54]

Overall, this spatial analysis catalogs potential regulators of OSNs projections or other spatially organized signaling pathways, providing a foundation for future functional experiments. To facilitate further exploration, we developed a web-based interface at or.merfisheyes.com where users can visualize the MOE distribution and OB projection of different OSN types and load the corresponding imputations for genes of interest.

High-throughput measure of specific odor responses in the MOE

Single-molecule FISH of immediate early genes (IEGs) (Figure 5A) combined with MERFISH for *ORs* enabled us to assess OSN responses in animals exposed to distinct olfactory cues. This paradigm was validated using acetophenone, whose *in vivo* OR response was previously characterized by multiple methods.[30,31] We first screened 12 putative IEGs (*Egr1*, *Fos*, *Npas4*, *Arc*, *Jun*, *Btg2*, *Fosb*, *Junb*, *Nr4a1*, *Nr4a2*, *Pcdh10*, *and Srxn1*)[44] (Figures S7A and S7B) and quantified the fraction of OSNs positive cells (>5 transcripts per cell) of each gene under 3 conditions: unstimulated condition (0%), and upon 1% and 100% acetophenone exposures (Figure S7C). *Egr1* and *Fos* showed the best performance with low baseline expression and concentration-dependent induction. At the single-OSN level, we saw good overlap (~75%) between OSNs that were *Egr1+* and OSNs that were IEG positive based on a combined z-score across the 6 best-performing IEGs (*Egr1*, *Fos*, *Junb*, *Btg2*, *Pch10*, and *Nr4a1*) (Figures S7D and S7E). Hence, we selected *Egr1* as the representative IEG to characterize the acetophenone response across OSN types.

Based on the number of *Egr1* transcripts in each OSN, we characterized the population-level responses for each OSN type to two concentrations of acetophenone—1% and 100% (Figures 5B–5D). Across *ORs* OSN populations exhibited three types of responses: (1) *strong response* (i.e., *Olfr430* and *Olfr983*), in which the majority of OSNs expressing the corresponding *ORs* were *Egr1+*, (2) *partial response* (i.e., *Ofr488* and *Olfr749*), in which a subpopulation of cells were *Egr1+*, and (3)

Figure 4. Integrating OSN spatial organization with scRNA-seq to reveal molecular patterns in the MOE and OB

(A) Schematic of imputation workflow: scRNA-seq[44] expression levels averaged across OSN types were mapped onto reference MOE sections and 3D OB projections. Distributions were denoised by spatial averaging (radius 50 μm for MOE; 400 μm for OB).

(B) Imputed expression of *Ncam2* and *Nqo1* used as validations. Expression levels are capped at the 95th percentile.

(C) UMAP embedding of imputed MOE patterns for the top ~5,000 differentially expressed genes. Proximity indicates higher spatial correlation. Genes were Leiden clustered as indicated.

(D and E) Example imputed MOE patterns for genes in the top branch (D; clusters 3, 8, 15) and the bottom branch (E; clusters 1, 2, 4, 5, 11) of the UMAP in (C).

(F) UMAP embedding of imputed OB patterns.

(G and H) Imputed OB patterns for genes shown in (D) and (E), respectively.

(I) Imputed patterns of example genes with similar MOE patterns but with divergent OB patterns.

(J and K) Gradient strength along D-V (J) and A-P (K) axes of OB imputations across axonal guidance/cell adhesion molecules. Genes are sorted by gradient strength. Insets show imputed patterns of example genes with strong gradients.

(L–O) Same as (J) and (K) for transcription factors and signaling molecules, respectively. Scale bars: 500 μm in (L), (N), and (O); 200 μm in (M).

See also Figures S5 and S6.

Please cite this article in press as: Bintu et al., Spatial organization and detection of social odors in mouse primary olfactory system, Cell (2026), https://doi.org/10.1016/j.cell.2026.03.053

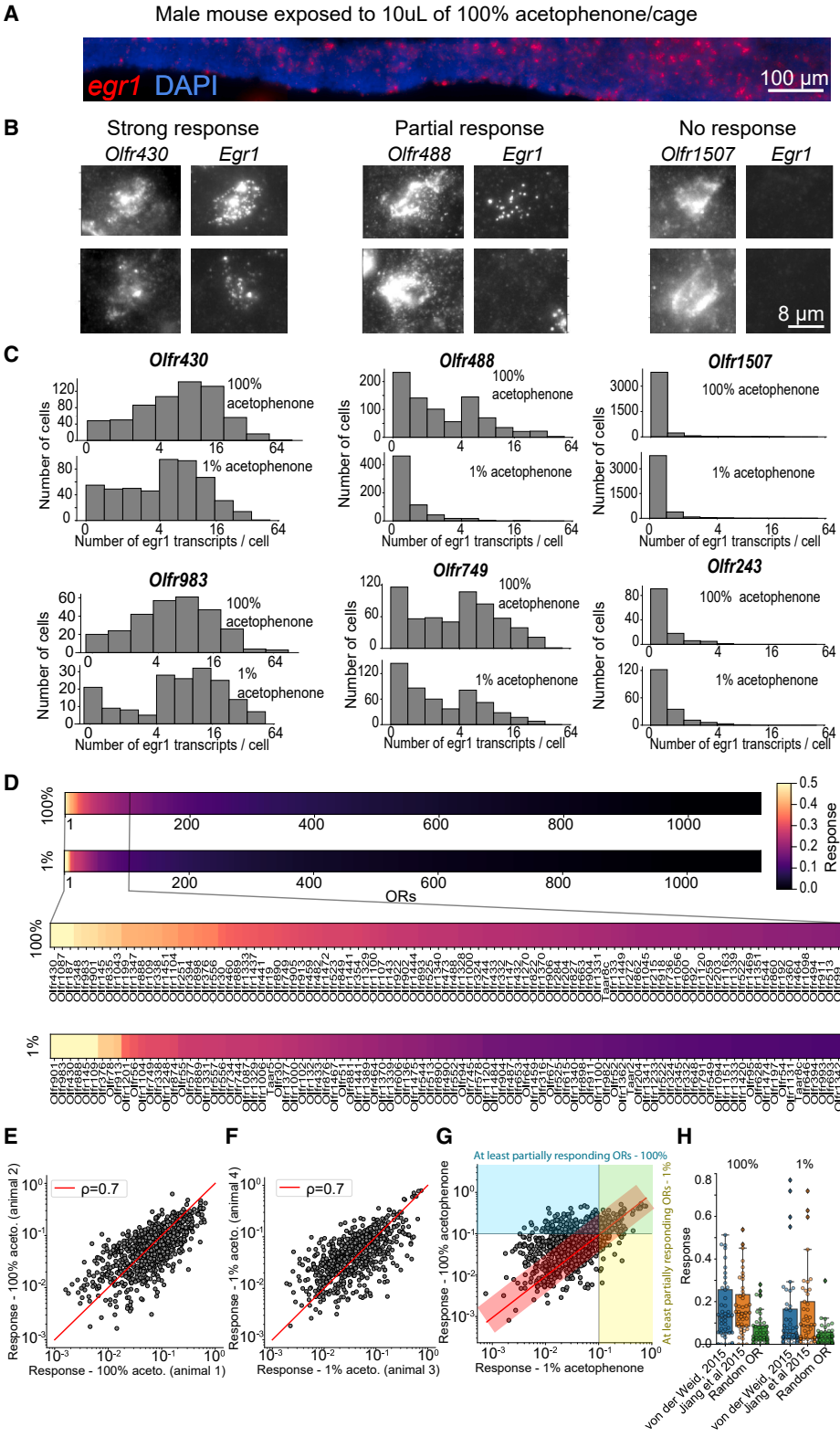

Figure 5. Cataloging OR responses to acetophenone

(A) High-magnification of MOE section showing *Egr1* transcripts (smFISH) marking neuronal activity following 30-min exposure to 100% acetophenone. Image is composed of aligned high-resolution tiles.

(legend continued on next page)

Please cite this article in press as: Bintu et al., Spatial organization and detection of social odors in mouse primary olfactory system, Cell (2026), https://doi.org/10.1016/j.cell.2026.03.053

no response (i.e., *Olfr1507* and *Olfr243*), in which almost all cells were *Egr1*−. The response of ORs to the cues was quantified as the fraction of *Egr1*$^+$ OSNs (>5 *Egr1* transcripts/cell) for each *OR* type (Figure 5D; Table S6). OR responses were reproducible across animals for both acetophenone concentrations (Figures 5E and 5F) (Pearson's correlation of ∼0.7). Increasing the concentration of acetophenone from 1% to 100% resulted in ∼2-fold higher number of ORs with strong or partial response, with 328 ORs showing enhanced response beyond replicate-to-replicate variability (Figure 5G). This demonstrates a concentration-dependent response at the population level of OSNs of different OR types.

Importantly, 7 of the 9 strongly responsive ORs (∼80%) were previously identified by orthogonal sequencing approaches[30,31] as responsive to acetophenone and, the other ORs identified in these studies showed statistically increased responses for both the high- and low-acetophenone concentrations compared with all other ORs (Wilcoxon test p values of 8.4×10^{-5} and 9.8×10^{-10} for 100% acetophenone and Wilcoxon test p values 3.6×10^{-5} and 4.4×10^{-7} for 1% acetophenone) (Figure 5H). Together, these results confirm that our imaging approach is suitable for measuring the response of the near-complete repertoire of ORs to specific odor molecules.

High-throughput measure of OSN responses to predator and social cues

We combined MERFISH with *Egr1* imaging to assess OSN responses to different ethological cues, including predator (i.e., cat bedding) and social cues (male, female, and pup intruders). We selected a 30-min exposure time to maximize IEG induction (Figure S7F). OR responses were averaged across 2–3 animals for each exposure covering: (1) males exposed to cat odor as a predator cue, (2) females exposed to male intruders, (3) males exposed to male intruders, (4) males exposed to female intruders, (5) females exposed to female intruders, (6) virgin females exposed to pups, and (7) mothers exposed to pups (Figure 6A; Table S7). As with acetophenone, we observed a reproducible (Pearson's correlation of ∼0.6–0.7 across replicates) graded response across all conditions: a small subset of ORs displayed a *strong response*, and 10–100 ORs displayed a varying degree of *partial response* (Figure 6A).

The responding sets of ORs, defined operationally for each cue as having at least a partial response (>0.1), were compared across the different cues and conditions. OR responses had the highest overlap for the same cue (male, female, or pup) regardless of the sex and parental experience of the exposed animal (Figure 6B), indicating that OSN responses were primarily determined by the odorant rather than by the internal state of the animal. ORs responding to male cue formed the largest and most selective set comprising 106 ORs, out of which 19% also responded to female cue (Figure 6C). In contrast, ORs responding to female cues constituted a more reduced set (34 ORs), with 60% also responding to male odor at a similar level. Notably, ORs categorized as male-selective had a statistically increased response to both sexes compared with all other ORs (p value = 3.34×10^{-5} Wilcoxon test) (Figure 6D) but were, nevertheless, 3–4 times more tuned to male compared with female odor. Similar results were observed for the female-selective ORs.

Pup cues elicited the most restricted response, comprising only 18 responsive ORs (Figure 6C). Strikingly, this response was modulated by the maternal state: mothers engaged all pup-responsive ORs identified in virgin females plus 11 additional, mother-selective ORs. ORs responding to pups in virgin females had approximately the same response level in mothers, whereas the mother-selective ORs were ∼4-fold higher tuned to pups in mothers compared with virgin females (Figure 6E). These data suggest that maternal experience selectively enhances the sensitivity of a specific subset of OSN types to pups.

The response of TAARs to ethological odors has been extensively investigated. *Taar5* was identified as strongly responding to male cues in both male and female mice, with *Taar5* deletion resulting in decreased sensitivity to male urine.[59–61] Consistent with these findings, our data indicate a strong response of *Taar5* to male cues together with a modest response to female and pup cues (Figure 6F). For each of the other cues tested, a different member of the Taar family had the strongest response (*Taar3* for female and *Taar7b* for pup cues), indicating that even across the narrower set of social cues and within the small family of TAARs, receptor responses are differently tuned to specific ethological cues.

The responsive ORs to each cue were more similar in sequence than expected by chance (Figure 6G) (Wilcoxon test; p values of 8.6×10^{-8}, 3.0×10^{-25}, 3.0×10^{-190}, and 8.2×10^{-3} for cat, female, male, and pup odors, respectively). However, larger OR clades or genomic clusters showed a heterogeneous response (Figures 6G and 6H). For instance, the phylogenetic clusters *Olfr1380-Olfr1390* responded primarily to male and female cues, while the neighboring cluster of *Olfr91-Olfr93* responded primarily to the cat cue. This heterogeneity is in contrast with the response of the vomeronasal V2R system[35] in which the phylogenetic clades of different V2Rs were highly sensitive to specific predatory/social cues.

(B) Representative images of three OSN response profiles: strong response (Olfr430; high *Egr1* in most cells), partial response (*Olfr488*; *Egr1* expression in a subpopulation), and no response (*Olfr1507*; minimal *Egr1* expression).
(C) Histograms of the number of *Egr1* transcripts per cell across example OSN types following exposure to 100% acetophenone (top) and 1% acetophenone (bottom).
(D) Catalogs of OR responses to 100% (top, $N = 3$) and 1% acetophenone (bottom, $N = 2$). OR responses were quantified as the fraction of OSNs of each OR-type expressing >5 *Egr1* transcripts.
(E and F) Correlation across replicates of OR responses to 100% (E) and 1% (F) acetophenone. Pearson correlation coefficients are indicated.
(G) Correlation between OR responses to 100% versus 1% acetophenone. The red line marks equal response, and the red-shaded region marks 90% confidence interval based on replicate variability. Guidelines mark 0.1 response to 100% (horizontal line) and 1% acetophenone (vertical line).
(H) Box and swarm plots of responses to 100% (left) and 1% (right) for two sets of 45 ORs previously identified as acetophenone-responding.[30,31] Responses for a control group of 45 randomly selected ORs are displayed for comparison.
See also Figure S7.

Please cite this article in press as: Bintu et al., Spatial organization and detection of social odors in mouse primary olfactory system, Cell (2026), https://doi.org/10.1016/j.cell.2026.03.053

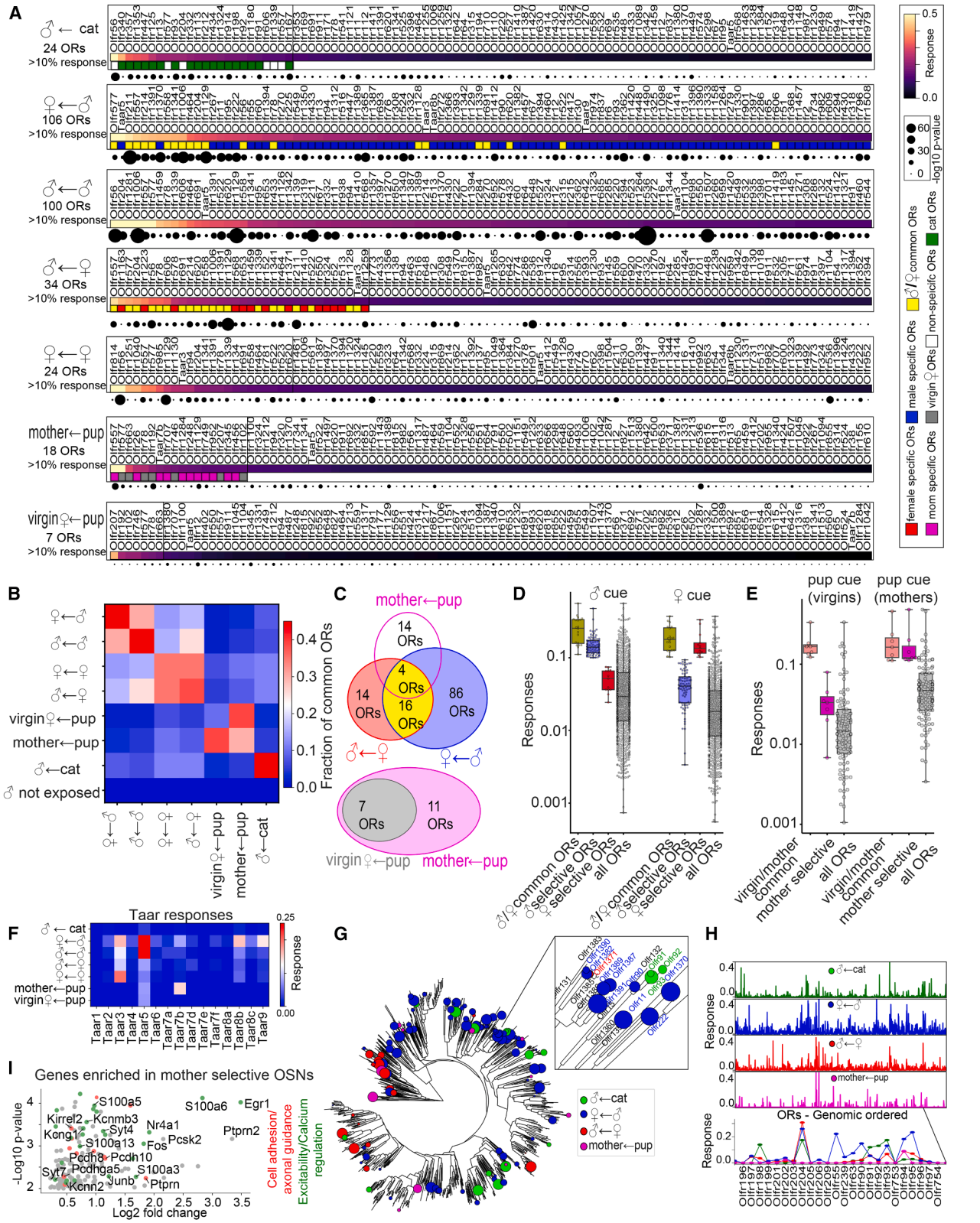

(legend on next page)

Please cite this article in press as: Bintu et al., Spatial organization and detection of social odors in mouse primary olfactory system, Cell (2026), https://doi.org/10.1016/j.cell.2026.03.053

To investigate the molecular basis of maternal pup responses, we searched for genes differentially expressed within mother-selective OSNs, defined as having a response greater than 0.05 in mothers and more than a 2-fold higher response in mothers compared with virgin females. We restricted the analysis to OSNs in scRNA-seq data originating from female animals and identified 156 genes with significant differential expression (p value < 0.01, Wilcoxon test, N = 8,308 cells) in mother-selective OSNs compared with all other OSNs. These genes predominantly fell into four categories: (1) axonal guidance molecules (i.e., *Kirrel2*, *Pcdh10*, *Pcdh8*, *Pcdhb18*, and *Pcdhga5*), potentially reflecting specialized projections of these OSNs (Figures S6I and S6J); (2) regulators of neuronal excitability (e.g., *Kcng1*, *Kcnn3*, and *Kctd1*), (3) regulators of calcium homeostasis including calcium-binding proteins (e.g., *S100a3*, *S100a5*, *S100a6*, and *S100a13*), and (4) IEGs (e.g., *Fos* and *Junb*) (Figure 6I). We note that the available scRNA-seq data did not allow further identification of genes with specific modulation between mother and virgin females since these two conditions were not profiled or annotated in this data.

Taken together, these experiments show a remarkable selectivity of OSN responses to ethologically relevant cues and activity modulation of specific OSNs in mothers.

Integrating functional and spatial information onto the epithelium and OB

We represented the OSN responses to each exposure condition within the spatial distribution map of the MOE and the projection map in the OB (Figures 7A–7D). The different classes of cues profiled corresponded to distinct spatial distributions both within the MOE and the OB. For example, receptors responding to cat cue were primarily enriched in a more peripheral ring in the MOE (Figure 7A) and projected primarily to a thin middle band within the OB with a higher density at the most anterior and most posterior regions (Figures 7C, 7E, and 7F). ORs responding to male odor were more broadly distributed across the MOE and projected primarily to two regions of the OB—a small dorsal region and a large mid-band along the D-V axis, spanning most of the A-P direction. ORs responding to female odor also covered a large area of the MOE, with preference to the central region, and projected to a few OB subdomains along the D-V axis and were more restricted to the mid-posterior region of the A-P axis. Finally, ORs responding to pup cues were concentrated primarily in the central MOE and projected to a small dorsal subdomain of the OB with a few scattered projections corresponding to ORs with a lower pup response. Notably, the dorsal subdomain covered the most responsive ORs in mothers compared with virgin females. These data begin to define a molecular and spatial organization of responsive OR domains within the MOE and OB and reveal the spatial specificity of ethologically relevant odor responses.

DISCUSSION

This study used multiplexed imaging to systematically quantify expression across the near-complete *OR* repertoire in both sensory neuron somas and axonal terminals. Two high-resolution and comprehensive molecular atlases were constructed, capturing the spatial distribution of sensory neurons within the MOE and their 3D projections into the OB. In the MOE, OSNs were organized at a larger scale into continuous rings of increasing diameter from the center to the periphery and at a smaller scale across continuous apical-basal layers. In the OB, the OR projection map was highly stereotypical across animals, with an average projection precision of 200–300 μm, equivalent to 2–3 glomeruli in diameter. This result aligns with prior functional work[22] showing that glomeruli can be matched across animals by their odor-response fingerprints with a precision of ∼200–300 μm, underscoring the high spatial and molecular precision of the OB map. An intriguing geometrical connection emerged upon comparing the MOE and OB atlases determined in this work: the preferential distributions of ORs along the central-peripheral and the apical-basal axes in the MOE are mapped onto the D-V and A-P projection axes of the OB, respectively.

These atlases provide a foundational resource for determining molecular mechanisms orchestrating the olfactory topography when integrated with existing or future molecular and functional studies. In this study, taking advantage of recent scRNA-seq

Figure 6. Cataloging OR responses to ethological cues

(A) Responses profiles for the top 100 ORs to seven olfactory stimulations: cat cue (sensed by N = 2 males), male cue (sensed by N = 2 females), male cue (sensed by N = 2 males), female cue (sensed by N = 2 males), female cue (sensed by N = 2 females), pup cue (sensed by N = 2 females), pup cue (sensed by N = 3 mothers) and pup cue (sensed by N = 3 virgin females). The ORs with >10% response, defined as *responding* ORs for each stimulation, are indicated. Colored squares mark non-selective ORs, responding to the majority of cues (white), cat-selective ORs (green), male-selective ORs (blue), female-selective ORs (red), ORs responding to both male and female cues (yellow), mother-selective ORs responding to pup (magenta), and ORs responding to pups in virgin females (gray). Dot plot underneath the responses of each OR quantifies the p value (Fisher's exact test) of the enriched response in each stimulation compared with the unstimulated condition.

(B) Pairwise overlap matrix of responsive ORs across exposure conditions. Diagonal elements quantify the fraction of common OR responses across replicates.

(C) Venn diagrams of ORs responding to social cues (top) and to the difference between maternal states for pup odor (bottom).

(D) Box and swarm plot of OR responses to male cue (sensed by females, left) and female cue (sensed by males, right) for: (1) common male and female responding ORs (yellow), (2) male-selective ORs (blue), (3) female-selective ORs (red), and (4) all ORs (light gray).

(E) Box and swarm plot of OR response to pup cue by virgin females (left) and by mothers (right) for: (1) common virgin and mother responding ORs (salmon), (2) mother-selective ORs (magenta), and (3) all ORs (light gray). Box plots indicate medians and 25^{th}/75^{th} percentiles; whiskers mark the minimum and maximum values.

(F) Plot with the responses of Taars across exposures.

(G) OR phylogenetic tree annotated with responses to 4 olfactory cues: cat odor (sensed by males, green), male cue (sensed by females, blue), female cue (sensed by males, red), and pup cue (sensed by mothers, magenta). Dot size is proportional to OR response. Inset: zoom in on a clade containing sub-branches Olfr1370-Olfr1390 and Olfr90-Olfr92.

(H) OR responses to 4 olfactory cues with the ORs sorted along the genomic axis. Inset: zoom in on the responses of a representative OR genomic cluster.

(I) Differential gene expression plot comparing mother-selective OSNs to all other OSNs, based on scRNA-seq.[44]

Please cite this article in press as: Bintu et al., Spatial organization and detection of social odors in mouse primary olfactory system, Cell (2026), https://doi.org/10.1016/j.cell.2026.03.053

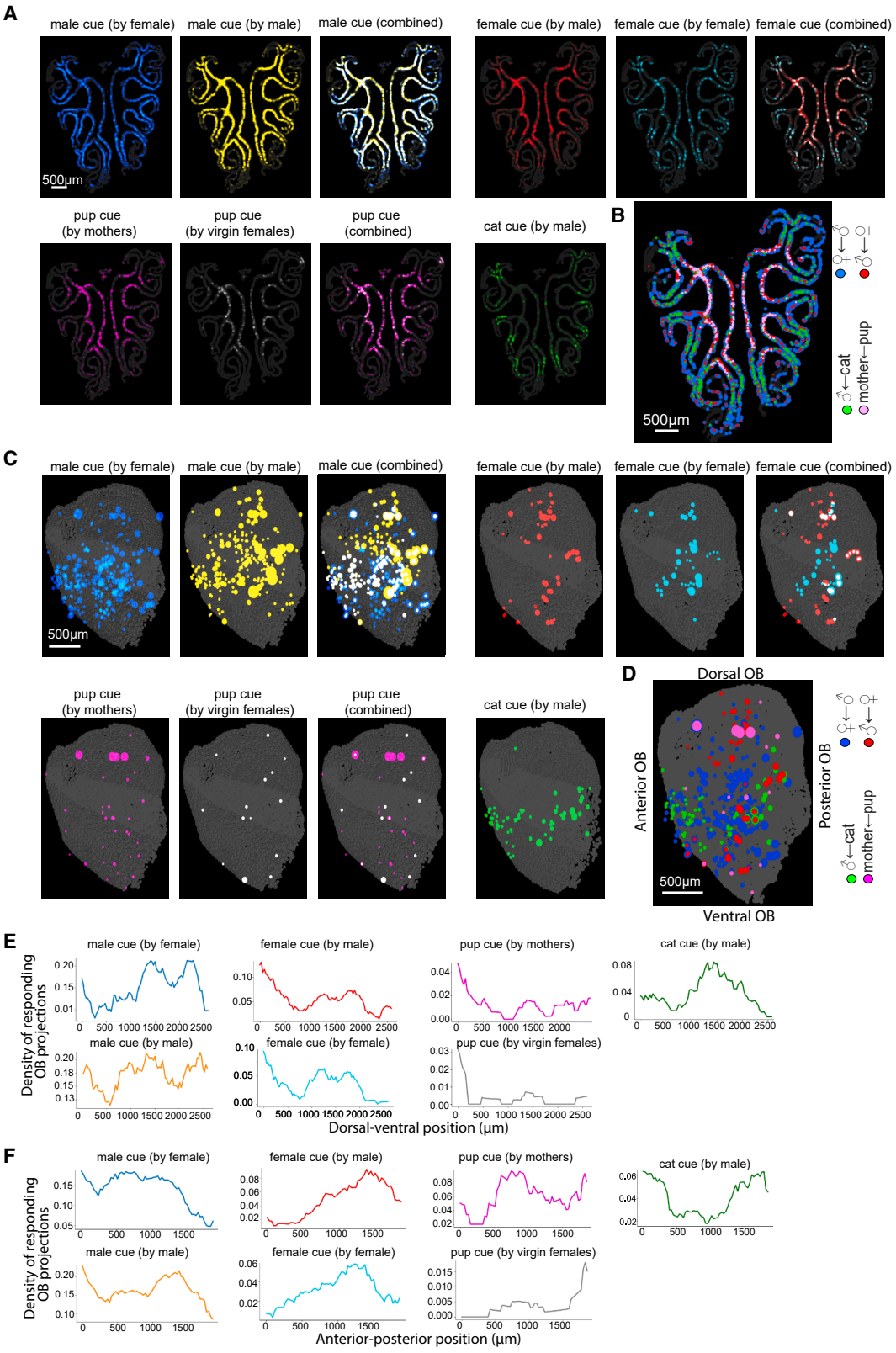

(legend on next page)

Please cite this article in press as: Bintu et al., Spatial organization and detection of social odors in mouse primary olfactory system, Cell (2026), https://doi.org/10.1016/j.cell.2026.03.053

datasets,[44,62,63] we began a preliminary investigation of the interplay between differential gene expression in OSNs, their precise spatial location in the MOE, and their axonal projections in the OB. We identified specific genes among transcription factors, axonal guidance, and signaling molecules that are expressed within neurons projecting to specific, contiguous subregions of the OB glomeruli layer. The differential expression of these genes supports a model in which specific transcription factors and signaling molecules cooperate to synchronize OR specification with appropriate axonal targeting signals.

Placing the spatial organization of sensory neurons within their functional context is a particularly exciting frontier that will strengthen previously developed methods to de-orphan receptors.[30,31] While most existing de-orphaning methods rely on monomolecular odorants at supraphysiological concentrations, our approach—coupling MERFISH with *Egr1* smFISH—functionally characterized OR responses to complex, physiologically relevant cues. The specific sets of responding ORs to each cue were cataloged and spatially mapped within the molecular atlases of the MOE and OB. This revealed the distinct spatial organization and projection of the responsive ORs, suggesting that odor information is mapped within constrained regions for localized processing. The response to male odor during direct interaction was found in OSNs projecting to a central band along the D-V axis of the OB and, to a lesser extent, to a dorsal subregion. This aligns with previous studies mapping IEG expression in the OB upon male urine exposure.[64] By contrast, responses to female odor were more enriched in OSNs projecting to the dorsal OB, which has been previously shown to be functionally critical for generating responses to female cues compared with male cues.[65] The response to cat predatory odor was localized primarily to OSNs projecting to a thin middle band encircling the OB. This finding, combined with the enrichment of pup-sensitive OSNs in the dorsal region of the OB, challenges a prior hypothesis that ventral regions of the OB encode attractive cues, whereas dorsal regions correspond to aversive cues.[1] The response to pup cue further revealed an increased sensitivity in a subset of OSN types in mothers compared with virgin females. While the prolactin signaling, whose modulatory role in females was recently described,[66] was not found to be enriched in mother-selective OSNs responding to pup cues (data not shown), we found other modulatory genes enriched in these OSNs, including genes involved in ion channel and calcium regulation. We note, however, that the number of cells in the single-cell sequencing data used to derive these gene enrichments is modest (~10,000 female OSNs) and hence certain modulatory genes might have been missed from this analysis. We also note that apart from transcriptional differences across OSNs, other factors could contribute to modulating OSN responses to social and predator odors, including, for instance, the animal's sampling duration when probing different ethologically relevant odors, the kinetics of the ORs, and their downstream signaling cascade. The identification of OSNs that selectively detect social and predator cues paves a new avenue to study the processing of distinct categories of innate main olfactory cues associated with dramatically different behavioral repertoires.

As the OR responses of more cues get characterized using either the imaging approach introduced here or other approaches, we anticipate that the spatial atlases provided here will help understand how the chemical environment gets progressively mapped across the olfactory circuit, including the epithelium and the OB.

Limitations of the study

Mechanisms orchestrating OSN spatial organization and axonal projection remain unresolved. Nevertheless, we anticipate that the comprehensive atlases of OSN distribution and projection presented here will help address this question when integrated with future molecular and functional studies. For instance, our preliminary exploration of scRNA-seq data mapped onto our spatial atlases highlighted specific axonal guidance molecules, transcription factors, and signaling molecules potentially involved in OSN localization and projection. Characterization of these genes is an emerging, yet incomplete effort,[48] which will be aided by the data provided in this work.

Connecting the spatial organization and projection of OSNs with their ethological sensing remains incomplete. Here we cataloged responses to one predatory cue (cat) and three social odors (male, female, and pups). Future studies will continue cataloging cues from food, nesting materials, or different predators and provide a more comprehensive understanding of how odor information is mapped across the olfactory circuitry.

While IEG expression serves as a proxy for neuronal activity, future integration of live calcium imaging will offer a more direct functional readout. Considering recent advances in recording Ca^{2+} activity within sensory neurons in chemosensory organs,[35,67] we envision that, after live recording, animals' OBs or MOEs can be dissected for MERFISH imaging of OR genes. While these experiments are technically challenging and can only provide access to a limited volume of the MOE/OB, they would provide a more direct connection, with more precise temporal dynamics, between the functional and molecular data, complementing the more comprehensive IEG-based measurements.

RESOURCE AVAILABILITY

Lead contact

Requests for further information and resources should be directed to and will be fulfilled by the lead contact, Catherine Dulac (dulac@fas.harvard.edu).

Figure 7. The spatial distribution and projection of the ORs responding to different olfactory cues

(A) Reference coronal MOE section with OR responses mapped to corresponding OSNs across stimulations. Transparency scale is proportional to the OR response.

(B) Composite image summarizing MOE spatial patterns of responses to different cues.

(C) OB projections annotated based on their corresponding OR response to different olfactory cues. Dot sizes are proportional to OR responses.

(D) Composite image summarizing the different OB spatial patterns of responses to different cues.

(E and F) Density distributions of responding OR projections for each stimulation along the D-V (E) and A-P (F) axis of the OB, binned in 200 μm intervals.

Materials availability

Oligonucleotide probe sequences used for MERFISH imaging can be found in Table S1. Templates and reagents for making these probes can be purchased from commercial sources, as detailed in the STAR Methods section.

Data and code availability

- Imaging data reported in this manuscript are publicly available at the Brain Knowledge Platform and Brain Image Library (https://knowledge.brain-map.org/data/KD2K0QPHBRWTNKYDUKB and https://knowledge.brain-map.org/data/7GQI8P3P8R40B6LPV9R).
- Analysis code used for MERFISH image decoding and data quantification is publicly available at Zenodo[68] (10.5281/zenodo.3758540).
- All original code associated with this manuscript has been deposited at Zenodo at 10.5281/zenodo.18948138 and at https://github.com/BogdanBintu/MERFISH_Analysis_Olfactory_Receptors and is publicly available as of the date of publication.
- Any additional information required to reanalyze the data reported in this paper is available from the lead contact upon request.

ACKNOWLEDGMENTS

This work was in part supported by the National Institute of Mental Health (U19MH114821 to X.Z. and C.D., R01HD082131 to C.D., and DP5-OD030878 to B.B.). X.Z. and C.D. are HHMI investigators. We thank Stacey Sullivan for helping with animal exposure to different cues, MCB Graphics from Harvard University for helping with figures, and Drs. Murphy, Kaplan, and Talay for helpful comments on the manuscript. We also thank Dr. Longzhi Tan for helpful discussions in designing the MERFISH probes targeting olfactory receptors and Dr. Yiqun Wang for help with the graphical abstract and comments on the manuscript.

AUTHOR CONTRIBUTIONS

B.B., Y.I., X.Z., and C.D. designed the study and interpreted the data. B.B. performed and analyzed experiments with inputs from Y.I. I.J. designed MERFISHEYES for data visualization. B.B., X.Z., and C.D. wrote the manuscript with input from all authors.

DECLARATION OF INTERESTS

X.Z. is an inventor of patents applied for by Harvard University related to MERFISH and is a co-founder and consultant of Vizgen, Inc.

STAR★METHODS

Detailed methods are provided in the online version of this paper and include the following:

- KEY RESOURCES TABLE
- EXPERIMENTAL MODEL AND STUDY PARTICIPANT DETAILS
  - Animals
- METHOD DETAILS
  - Oligonucleotide Probe design
  - Assigning the MERFISH readout sequences using a split-amplifier strategy
  - Sample preparation and hybridization
  - MERFISH decoding of OR identity of sensory neurons in the MOE
  - Imaging and aligning the OB sections
  - MERFISH decoding of OR identity of glomeruli in the OB
- QUANTIFICATION AND STATISTICAL ANALYSIS
  - Correlation analysis
  - Statistical tests
  - Estimating the relative contributions of genomic distance and sequence similarity of ORs to the spatial overlap of their OSNs

SUPPLEMENTAL INFORMATION

Supplemental information can be found online at https://doi.org/10.1016/j.cell.2026.03.053.

Received: April 27, 2025
Revised: December 1, 2025
Accepted: March 30, 2026

REFERENCES

1. Mori, K., and Sakano, H. (2021). Olfactory circuitry and behavioral decisions. Annu. Rev. Physiol. *83*, 231–256. https://doi.org/10.1146/annurev-physiol-031820-092824.
2. Murthy, V.N. (2011). Olfactory maps in the brain. Annu. Rev. Neurosci. *34*, 233–258. https://doi.org/10.1146/annurev-neuro-061010-113738.
3. Monahan, K., and Lomvardas, S. (2015). Monoallelic expression of olfactory receptors. Annu. Rev. Cell Dev. Biol. *31*, 721–740. https://doi.org/10.1146/annurev-cellbio-100814-125308.
4. Lomvardas, S., and Maniatis, T. (2016). Histone and DNA Modifications as Regulators of Neuronal Development and Function. Cold Spring Harb. Perspect. Biol. *8*, a024208. https://doi.org/10.1101/cshperspect.a024208.
5. Monahan, K., Horta, A., and Lomvardas, S. (2019). LHX2- and LDB1-mediated trans interactions regulate olfactory receptor choice. Nature *565*, 448–453. https://doi.org/10.1038/s41586-018-0845-0.
6. Tan, L., Xie, X.S., and Lomvardas, S. (2025). Genomic snowflakes: how the uniqueness of DNA folding allows us to smell the chemical universe. Curr. Opin. Genet. Dev. *92*, 102329. https://doi.org/10.1016/j.gde.2025.102329.
7. Buck, L., and Axel, R. (1991). A novel multigene family may encode odorant receptors: a molecular basis for odor recognition. Cell *65*, 175–187. https://doi.org/10.1016/0092-8674(91)90418-X.
8. Chess, A., Simon, I., Cedar, H., and Axel, R. (1994). Allelic inactivation regulates olfactory receptor gene expression. Cell *78*, 823–834. https://doi.org/10.1016/S0092-8674(94)90562-2.
9. Vassar, R., Chao, S.K., Sitcheran, R., Nuñez, J.M., Vosshall, L.B., and Axel, R. (1994). Topographic organization of sensory projections to the olfactory bulb. Cell *79*, 981–991. https://doi.org/10.1016/0092-8674(94)90029-9.
10. Ressler, K.J., Sullivan, S.L., and Buck, L.B. (1994). Information coding in the olfactory system: evidence for a stereotyped and highly organized epitope map in the olfactory bulb. Cell *79*, 1245–1255. https://doi.org/10.1016/0092-8674(94)90015-9.
11. Mombaerts, P., Wang, F., Dulac, C., Chao, S.K., Nemes, A., Mendelsohn, M., Edmondson, J., and Axel, R. (1996). Visualizing an olfactory sensory map. Cell *87*, 675–686. https://doi.org/10.1016/S0092-8674(00)81387-2.
12. Ressler, K.J., Sullivan, S.L., and Buck, L.B. (1993). A zonal organization of odorant receptor gene expression in the olfactory epithelium. Cell *73*, 597–609. https://doi.org/10.1016/0092-8674(93)90145-G.
13. Vassar, R., Ngai, J., and Axel, R. (1993). Spatial segregation of odorant receptor expression in the mammalian olfactory epithelium. Cell *74*, 309–318. https://doi.org/10.1016/0092-8674(93)90422-M.
14. Zapiec, B., and Mombaerts, P. (2020). The zonal organization of odorant receptor gene choice in the main olfactory epithelium of the mouse. Cell Rep. *30*, 4220–4234.e5. https://doi.org/10.1016/j.celrep.2020.02.110.
15. Miyamichi, K., Serizawa, S., Kimura, H.M., and Sakano, H. (2005). Continuous and overlapping expression domains of odorant receptor genes in the olfactory epithelium determine the dorsal/ventral positioning of glomeruli in the olfactory bulb. J. Neurosci. *25*, 3586–3592. https://doi.org/10.1523/JNEUROSCI.0324-05.2005.
16. Tan, L., and Xie, X.S. (2018). A near-complete spatial map of olfactory receptors in the mouse main olfactory epithelium. Chem. Senses *43*, 427–432. https://doi.org/10.1093/chemse/bjy030.

17. Ruiz Tejada Segura, M.L., Abou Moussa, E., Garabello, E., Nakahara, T.S., Makhlouf, M., Mathew, L.S., Wang, L., Valle, F., Huang, S.S.Y., Mainland, J.D., et al. (2022). A 3D transcriptomics atlas of the mouse nose sheds light on the anatomical logic of smell. Cell Rep. *38*, 110547. https://doi.org/10.1016/j.celrep.2022.110547.

18. Zapiec, B., and Mombaerts, P. (2015). Multiplex assessment of the positions of odorant receptor-specific glomeruli in the mouse olfactory bulb by serial two-photon tomography. Proc. Natl. Acad. Sci. USA *112*, E5873–E5882. https://doi.org/10.1073/pnas.1512135112.

19. Pacifico, R., Dewan, A., Cawley, D., Guo, C., and Bozza, T. (2012). An olfactory subsystem that mediates high-sensitivity detection of volatile amines. Cell Rep. *2*, 76–88. https://doi.org/10.1016/j.celrep.2012.06.006.

20. Wang, I.-H., Murray, E., Andrews, G., Jiang, H.-C., Park, S.J., Donnard, E., Durán-Laforet, V., Bear, D.M., Faust, T.E., Garber, M., et al. (2022). Spatial transcriptomic reconstruction of the mouse olfactory glomerular map suggests principles of odor processing. Nat. Neurosci. *25*, 484–492. https://doi.org/10.1038/s41593-022-01030-8.

21. Zhu, K.W., Burton, S.D., Nagai, M.H., Silverman, J.D., de March, C.A., Wachowiak, M., and Matsunami, H. (2022). Decoding the olfactory map through targeted transcriptomics links murine olfactory receptors to glomeruli. Nat. Commun. *13*, 5137. https://doi.org/10.1038/s41467-022-32267-3.

22. Soucy, E.R., Albeanu, D.F., Fantana, A.L., Murthy, V.N., and Meister, M. (2009). Precision and diversity in an odor map on the olfactory bulb. Nat. Neurosci. *12*, 210–220. https://doi.org/10.1038/nn.2262.

23. Rubin, B.D., and Katz, L.C. (1999). Optical imaging of odorant representations in the mammalian olfactory bulb. Neuron *23*, 499–511. https://doi.org/10.1016/S0896-6273(00)80803-X.

24. Belluscio, L., and Katz, L.C. (2001). Symmetry, stereotypy, and topography of odorant representations in mouse olfactory bulbs. J. Neurosci. *21*, 2113–2122. https://doi.org/10.1523/JNEUROSCI.21-06-02113.2001.

25. Meister, M., and Bonhoeffer, T. (2001). Tuning and topography in an odor map on the rat olfactory bulb. J. Neurosci. *21*, 1351–1360. https://doi.org/10.1523/JNEUROSCI.21-04-01351.2001.

26. Wachowiak, M., Denk, W., and Friedrich, R.W. (2004). Functional organization of sensory input to the olfactory bulb glomerulus analyzed by two-photon calcium imaging. Proc. Natl. Acad. Sci. USA *101*, 9097–9102. https://doi.org/10.1073/pnas.0400438101.

27. Mori, K., Takahashi, Y.K., Igarashi, K.M., and Yamaguchi, M. (2006). Maps of odorant molecular features in the Mammalian olfactory bulb. Physiol. Rev. *86*, 409–433. https://doi.org/10.1152/physrev.00021.2005.

28. Ma, L., Qiu, Q., Gradwohl, S., Scott, A., Yu, E.Q., Alexander, R., Wiegraebe, W., and Yu, C.R. (2012). Distributed representation of chemical features and tunotopic organization of glomeruli in the mouse olfactory bulb. Proc. Natl. Acad. Sci. USA *109*, 5481–5486. https://doi.org/10.1073/pnas.1117491109.

29. Peterlin, Z., Firestein, S., and Rogers, M.E. (2014). The state of the art of odorant receptor deorphanization: a report from the orphanage. J. Gen. Physiol. *143*, 527–542. https://doi.org/10.1085/jgp.201311151.

30. Jiang, Y., Gong, N.N., Hu, X.S., Ni, M.J., Pasi, R., and Matsunami, H. (2015). Molecular profiling of activated olfactory neurons identifies odorant receptors for odors in vivo. Nat. Neurosci. *18*, 1446–1454. https://doi.org/10.1038/nn.4104.

31. von der Weid, B., Rossier, D., Lindup, M., Tuberosa, J., Widmer, A., Col, J.D., Kan, C., Carleton, A., and Rodriguez, I. (2015). Large-scale transcriptional profiling of chemosensory neurons identifies receptor-ligand pairs in vivo. Nat. Neurosci. *18*, 1455–1463. https://doi.org/10.1038/nn.4100.

32. Vihani, A., Hu, X.S., Gundala, S., Koyama, S., Block, E., and Matsunami, H. (2020). Semiochemical responsive olfactory sensory neurons are sexually dimorphic and plastic. eLife *9*, e54501. https://doi.org/10.7554/eLife.54501.

33. Hu, X.S., Ikegami, K., Vihani, A., Zhu, K.W., Zapata, M., de March, C.A., Do, M., Vaidya, N., Kucera, G., Bock, C., et al. (2020). Concentration-dependent recruitment of mammalian odorant receptors. eNeuro *7*, ENEURO.0103-19.2019. https://doi.org/10.1523/ENEURO.0103-19.2019.

34. Chen, K.H., Boettiger, A.N., Moffitt, J.R., Wang, S., and Zhuang, X. (2015). RNA imaging. Spatially resolved, highly multiplexed RNA profiling in single cells. Science *348*, aaa6090. https://doi.org/10.1126/science.aaa6090.

35. Isogai, Y., Si, S., Pont-Lezica, L., Tan, T., Kapoor, V., Murthy, V.N., and Dulac, C. (2011). Molecular organization of vomeronasal chemoreception. Nature *478*, 241–245. https://doi.org/10.1038/nature10437.

36. van der Linden, C., Jakob, S., Gupta, P., Dulac, C., and Santoro, S.W. (2018). Sex separation induces differences in the olfactory sensory receptor repertoires of male and female mice. Nat. Commun. *9*, 5081. https://doi.org/10.1038/s41467-018-07120-1.

37. Moffitt, J.R., Bambah-Mukku, D., Eichhorn, S.W., Vaughn, E., Shekhar, K., Perez, J.D., Rubinstein, N.D., Hao, J., Regev, A., Dulac, C., et al. (2018). Molecular, spatial, and functional single-cell profiling of the hypothalamic preoptic region. Science *362*, eaau5324. https://doi.org/10.1126/science.aau5324.

38. Xia, C., Fan, J., Emanuel, G., Hao, J., and Zhuang, X. (2019). Spatial transcriptome profiling by MERFISH reveals subcellular RNA compartmentalization and cell cycle-dependent gene expression. Proc. Natl. Acad. Sci. USA *116*, 19490–19499. https://doi.org/10.1073/pnas.1912459116.

39. Fang, R., Xia, C., Close, J.L., Zhang, M., He, J., Huang, Z., Halpern, A.R., Long, B., Miller, J.A., Lein, E.S., et al. (2022). Conservation and divergence of cortical cell organization in human and mouse revealed by MERFISH. Science *377*, 56–62. https://doi.org/10.1126/science.abm1741.

40. Ibarra-Soria, X., Levitin, M.O., Saraiva, L.R., and Logan, D.W. (2014). The olfactory transcriptomes of mice. PLoS Genet. *10*, e1004593. https://doi.org/10.1371/journal.pgen.1004593.

41. Goh, J.J.L., Chou, N., Seow, W.Y., Ha, N., Cheng, C.P.P., Chang, Y.-C., Zhao, Z.W., and Chen, K.H. (2020). Highly specific multiplexed RNA imaging in tissues with split-FISH. Nat. Methods *17*, 689–693. https://doi.org/10.1038/s41592-020-0858-0.

42. Xia, C., Babcock, H.P., Moffitt, J.R., and Zhuang, X. (2019). Multiplexed detection of RNA using MERFISH and branched DNA amplification. Sci. Rep. *9*, 7721. https://doi.org/10.1038/s41598-019-43943-8.

43. Vassalli, A., Rothman, A., Feinstein, P., Zapotocky, M., and Mombaerts, P. (2002). Minigenes impart odorant receptor-specific axon guidance in the olfactory bulb. Neuron *35*, 681–696. https://doi.org/10.1016/S0896-6273(02)00793-6.

44. Tsukahara, T., Brann, D.H., Pashkovski, S.L., Guitchounts, G., Bozza, T., and Datta, S.R. (2021). A transcriptional rheostat couples past activity to future sensory responses. Cell *184*, 6326–6343.e32. https://doi.org/10.1016/j.cell.2021.11.022.

45. Markenscoff-Papadimitriou, E., Allen, W.E., Colquitt, B.M., Goh, T., Murphy, K.K., Monahan, K., Mosley, C.P., Ahituv, N., and Lomvardas, S. (2014). Enhancer interaction networks as a means for singular olfactory receptor expression. Cell *159*, 543–557. https://doi.org/10.1016/j.cell.2014.09.033.

46. Pyrski, M., Xu, Z., Walters, E., Gilbert, D.J., Jenkins, N.A., Copeland, N.G., and Margolis, F.L. (2001). The OMP-lacZ transgene mimics the unusual expression pattern of OR-Z6, a new odorant receptor gene on mouse chromosome 6: implication for locus-dependent gene expression. J. Neurosci. *21*, 4637–4648. https://doi.org/10.1523/JNEUROSCI.21-13-04637.2001.

47. Wang, Y., Sun, Y., and Joseph, P.V. (2023). Diverse evolutionary rates and gene duplication patterns among families of functional olfactory receptor genes in humans. PLoS One *18*, e0282575. https://doi.org/10.1371/journal.pone.0282575.

48. Bashkirova, E.V., Klimpert, N., Monahan, K., Campbell, C.E., Osinski, J., Tan, L., Schieren, I., Pourmorady, A., Stecky, B., Barnea, G., et al. (2023). Opposing, spatially-determined epigenetic forces impose restrictions on stochastic olfactory receptor choice. eLife *12*, RP87445. https://doi.org/10.7554/eLife.87445.

49. Stringer, C., Wang, T., Michaelos, M., and Pachitariu, M. (2021). Cellpose: a generalist algorithm for cellular segmentation. Nat. Methods *18*, 100–106. https://doi.org/10.1038/s41592-020-01018-x.

50. Yang, J., Shi, P., Li, Y., Zuo, Y., Nie, Y., Xu, T., Peng, D., An, Z., Huang, T., Zhang, J., et al. (2024). Regulatory mechanisms orchestrating cellular diversity of Cd36+ olfactory sensory neurons revealed by scRNA-seq and scATAC-seq analysis. Cell Rep. *43*, 114671. https://doi.org/10.1016/j.celrep.2024.114671.

51. Coleman, J.H., Lin, B., Louie, J.D., Peterson, J., Lane, R.P., and Schwob, J.E. (2019). Spatial determination of neuronal diversification in the olfactory epithelium. J. Neurosci. *39*, 814–832. https://doi.org/10.1523/JNEUROSCI.3594-17.2018.

52. Mountoufaris, G., Chen, W.V., Hirabayashi, Y., O'Keeffe, S., Chevee, M., Nwakeze, C.L., Polleux, F., and Maniatis, T. (2017). Multicluster Pcdh diversity is required for mouse olfactory neural circuit assembly. Science *356*, 411–414. https://doi.org/10.1126/science.aai8801.

53. Gene Ontology Consortium (2010). The Gene Ontology in 2010: extensions and refinements. Nucleic Acids Res. *38*, D331–D335. https://doi.org/10.1093/nar/gkp1018.

54. Sakano, H. (2020). Developmental regulation of olfactory circuit formation in mice. Dev. Growth Differ. *62*, 199–213. https://doi.org/10.1111/dgd.12657.

55. Assens, A., Dal Col, J.A., Njoku, A., Dietschi, Q., Kan, C., Feinstein, P., Carleton, A., and Rodriguez, I. (2016). Alteration of Nrp1 signaling at different stages of olfactory neuron maturation promotes glomerular shifts along distinct axes in the olfactory bulb. Development *143*, 3817–3825. https://doi.org/10.1242/dev.138941.

56. Cho, J.H., Kam, J.W.K., and Cloutier, J.-F. (2012). Slits and Robo-2 regulate the coalescence of subsets of olfactory sensory neuron axons within the ventral region of the olfactory bulb. Dev. Biol. *371*, 269–279. https://doi.org/10.1016/j.ydbio.2012.08.028.

57. McIntyre, J.C., Titlow, W.B., and McClintock, T.S. (2010). Axon growth and guidance genes identify nascent, immature, and mature olfactory sensory neurons. J. Neurosci. Res. *88*, 3243–3256. https://doi.org/10.1002/jnr.22497.

58. Mosca, T.J., and Luo, L. (2014). Synaptic organization of the Drosophila antennal lobe and its regulation by the Teneurins. eLife *3*, e03726. https://doi.org/10.7554/eLife.03726.

59. Liberles, S.D., and Buck, L.B. (2006). A second class of chemosensory receptors in the olfactory epithelium. Nature *442*, 645–650. https://doi.org/10.1038/nature05066.

60. Dewan, A., Pacifico, R., Zhan, R., Rinberg, D., and Bozza, T. (2013). Non-redundant coding of aversive odours in the main olfactory pathway. Nature *497*, 486–489. https://doi.org/10.1038/nature12114.

61. Li, Q., Korzan, W.J., Ferrero, D.M., Chang, R.B., Roy, D.S., Buchi, M., Lemon, J.K., Kaur, A.W., Stowers, L., Fendt, M., et al. (2013). Synchronous evolution of an odor biosynthesis pathway and behavioral response. Curr. Biol. *23*, 11–20. https://doi.org/10.1016/j.cub.2012.10.047.

62. Hanchate, N.K., Kondoh, K., Lu, Z., Kuang, D., Ye, X., Qiu, X., Pachter, L., Trapnell, C., and Buck, L.B. (2015). Single-cell transcriptomics reveals receptor transformations during olfactory neurogenesis. Science *350*, 1251–1255. https://doi.org/10.1126/science.aad2456.

63. Saraiva, L.R., Ibarra-Soria, X., Khan, M., Omura, M., Scialdone, A., Mombaerts, P., Marioni, J.C., and Logan, D.W. (2015). Hierarchical deconstruction of mouse olfactory sensory neurons: from whole mucosa to single-cell RNA-seq. Sci. Rep. *5*, 18178. https://doi.org/10.1038/srep18178.

64. Schaefer, M.L., Yamazaki, K., Osada, K., Restrepo, D., and Beauchamp, G.K. (2002). Olfactory fingerprints for major histocompatibility complex-determined body odors II: Relationship among odor maps, genetics, odor composition, and behavior. J. Neurosci. *22*, 9513–9521. https://doi.org/10.1523/JNEUROSCI.22-21-09513.2002.

65. Matsuo, T., Hattori, T., Asaba, A., Inoue, N., Kanomata, N., Kikusui, T., Kobayakawa, R., and Kobayakawa, K. (2015). Genetic dissection of pheromone processing reveals main olfactory system-mediated social behaviors in mice. Proc. Natl. Acad. Sci. USA *112*, E311–E320. https://doi.org/10.1073/pnas.1416723112.

66. Aoki, M., Gamayun, I., Wyatt, A., Grünewald, R., Simon-Thomas, M., Philipp, S.E., Hummel, O., Wagenpfeil, S., Kattler, K., Gasparoni, G., et al. (2021). Prolactin-sensitive olfactory sensory neurons regulate male preference in female mice by modulating responses to chemosensory cues. Sci. Adv. *7*, eabg4074. https://doi.org/10.1126/sciadv.abg4074.

67. Lee, D., Kume, M., and Holy, T.E. (2019). Sensory coding mechanisms revealed by optical tagging of physiologically defined neuronal types. Science *366*, 1384–1389. https://doi.org/10.1126/science.aax8055.

68. Emanuel, G., seichhorn, Babcock, H., leonardosepulveda, and timblosser. (2020). ZhuangLab/MERlin: MERlin v0.1.6. Zenodo. https://doi.org/10.5281/ZENODO.3758540.

69. Su, J.-H., Zheng, P., Kinrot, S.S., Bintu, B., and Zhuang, X. (2020). Genome-scale imaging of the 3D organization and transcriptional activity of chromatin. Cell *182*, 1641–1659.e26. https://doi.org/10.1016/j.cell.2020.07.032.

70. Bintu, B., Mateo, L.J., Su, J.-H., Sinnott-Armstrong, N.A., Parker, M., Kinrot, S., Yamaya, K., Boettiger, A.N., and Zhuang, X. (2018). Super-resolution chromatin tracing reveals domains and cooperative interactions in single cells. Science *362*, eaau1783. https://doi.org/10.1126/science.aau1783.

Please cite this article in press as: Bintu et al., Spatial organization and detection of social odors in mouse primary olfactory system, Cell (2026), https://doi.org/10.1016/j.cell.2026.03.053

CellPress
OPEN ACCESS

STAR★METHODS

KEY RESOURCES TABLE

REAGENT or RESOURCE	SOURCE	IDENTIFIER
Chemicals, peptides, and recombinant proteins		
Formamide	Ambion	Cat# AM9342
20xSSC	Ambion	Cat# AM9763
Triton-X	Sigma	Cat# T8787
Glucose oxidase	Sigma	Cat# G2133
EDTA	Boston Bioproducts	Cat# BM-150
EvaGreen Dye, 20x	Biotium	Cat# 31000
Phusion® Hot Start Flex 2X Master Mix	New England Biolabs	Cat# M0536
HiScribe T7 Quick High Yield RNA Synthesis Kit	New England Biolabs	Cat# E2050
Maxima H Minus Reverse Transcriptase	ThermoFisher	Cat# EP0752
dNTP mix	ThermoFisher	Cat# R1121
Fibronectin Bovine Plasma	Sigma	Cat# F1141
32% Paraformaldehyde	Fisher Scientific	Cat# 50-980-494
Dextran Sulfate	Sigma	Cat# D8906
DAPI	ThermoFisher	Cat# D1306
RNase inhibitor, Murine	New England Biolabs	Cat# M0314
RNasin Plus RNase Inhibitor	Fisher Scientific	Cat# PRN2615
1M Tris, pH 8	ThermoFisher	Cat# 15568025
Catalase	Sigma	Cat# C3155
6-hydroxy-2,5,7,8-tetramethylchroman-2-carboxylic acid (Trolox)	Sigma	Cat# 238813
tris(2-carboxyethyl)phosphine (TCEP)	Sigma	Cat# C4706
Tween-20	Sigma	Cat# P9416
Acetophenone	Sigma	Cat# A10701-5ML
Experimental models: Organisms/strains		
Mouse: C57BL/6J	The Jackson Laboratory	JAX: 000664; RRID:IMSR_JAX:000664
Mouse: CD-1	Charles River Laboratories	Crl:CD1(ICR) 022
Mouse: Olfr17-IRES-tau-lacZ	Richard Axel	JAX: 007767; RRID:IMSR_JAX:007767
Mouse: Olfr16-IRES-tau-GFP	Richard Axel	JAX: 006643; RRID:IMSR_JAX:006643
Oligonucleotides		
Primers, readout probes and adaptor probes	Integrated DNA Technologies, Bio-Synthesis Inc.	See Table S1
Primary/encoding oligonucleotide probe libraries	Twist Bioscience	See Table S1
Software and algorithms		
Software for analyzing multiplexed FISH data	This paper	Zenodo: https://doi.org/10.5281/zenodo.18948138
Deposited data		
Multiplexed FISH data	This paper	Brain Image Library: https://knowledge.brain-map.org/data/KD2K0QPHBRWTNKYDUKB; https://knowledge.brain-map.org/data/7GQI8P3P8R40B6LPV9R
snRNA-seq	PMID: 34879231	GEO: GSE173947
OR zonal information	PMID: 29796642	Tables S4 and S5

Please cite this article in press as: Bintu et al., Spatial organization and detection of social odors in mouse primary olfactory system, Cell (2026), https://doi.org/10.1016/j.cell.2026.03.053

EXPERIMENTAL MODEL AND STUDY PARTICIPANT DETAILS

Animals

C57BL/6J and CD1 mice were obtained from Jackson Laboratories and Charles River Laboratories respectively.

Adult C57BL/6J (8-11 week-old) male mice (N=4) were used for acetophenone exposures.

Adult (8-11 week-old) CD1 male (N=6) and CD1 female (N=10) mice were used for predator and social cue exposures.

8-week old Olfr17-IRES-tau-lacZ and Olfr16-IRES-tau-GFP male mice (N=1 each) were used to validate MERFISH quantifications. These strains were obtained from Dr. Richard Axel's lab.

Mouse husbandry and experiments were performed following institutional and federal guidelines and were approved by Harvard University's Institutional Animal Care and Use Committee.

METHOD DETAILS

Oligonucleotide Probe design

The design of the MERFISH probes targeting the olfactory receptor genes followed a similar design as previously described[69] with a few notable modifications.

Briefly, the probes were synthesized from a pool of oligonucleotides purchased from Twist Biosciences. Each oligo in this pool consisted of the following sub-sequences (from 5' to 3'):

1. A 20-nt or 19-nt forward priming region for PCR amplification
2. A 20-nt priming sequence used for the RT reaction during synthesis
3. A 15-nt 5' split readout sequence used for developing the MERFISH signal
4. A 30-32-nt target sequence complementary to the olfactory receptor transcripts
5. A 15-nt 3' split readout sequence used for developing the MERFISH signal
6. A 20-nt or 19-nt reverse priming sequence for PCR amplification

The target sequences were also screened using a similar procedure as in[69] with the additional feature that we allowed the length to vary between 30-32 nt to increase the number of neighboring pairs of probes. Moreover, to increase the specificity of the target sequences to the OR of interest, we designed probes against the enlarged annotations of the olfactory receptor transcripts.[40]

Assigning the MERFISH readout sequences using a split-amplifier strategy

For every pair of adjacent probes targeting the OR transcripts we assigned a unique MERFISH bit by first designing a specific 5' split readout sequence to the 3' probe in the pair and a 3' split readout sequence to the 5' probe in the pair (see Figure S1 for details). The 3' and 5' pair split readout sequences together formed a single 30-nt readout binding sequence when the pair of probes are in proximity (i.e bound to the target transcript). A total of 15 pairs of 3'-5' split readout sequences were designed - each corresponding to 1 of the 15 MERFISH bits. A unique set of 4 out of 15 3'-5' pairs of split readout sequences were associated with the probes targeting each OR transcript. Each of these sequence pairs were repeated for each transcript 4-10 times.

190-nt probes (IDT), called preamplifier probes, were designed to contain a 30-nt sequence complementary to the concatenated pair of split readout probes. The remaining sequence contained 8 repeats of a 20-nt binding site. A total of 15 preamplifier probes were uniquely designed and correspond to each of the 15 MERFISH bits.

200-nt probes (IDT) called amplifier probes were designed to contain a 20-nt sequence complementary to the repeated binding site on each preamplifier probe and 9 repeats of another 20-nt binding site. A total of 15 preamplifier probes were uniquely designed to bind to each of the preamplifier probes and correspond to each of the 15 MERFISH bits.

30-nt fluorescent readout probes (IDT) were designed to contain a 20-nt sequence complementary to the repeated binding site on the amplifier probe. 15 readout sequences were designed to bind each amplifier probes and corresponded to each of the 15 MERFISH bits.

The *Egr1* probes were designed in a similar manner with a unique pair of 3'-5' split readout probes and unique preamplifier, amplifier and readout probes. The Egr1 signal was first labelled and imaged across the sections, quenched and then the MERFISH readout probes were sequentially hybridized and imaged in 2-3 colors.

To quench the fluorescent signal after each imaging round we used a toehold displacement strategy (as described previously[70]) in which unlabeled probes (IDT) complementary to the readout probes unhybridized the readout probes from the amplifier binding sites.

Sample preparation and hybridization

The cryosectioning, the hybridization of the encoding probe and the gel embedding and clearing of the sample were performed as described previously.[37]

To fluorescently label the transcripts and amplify the signal, the preamplifier and amplifier probes were sequentially hybridized to the sample through the following protocol:

Please cite this article in press as: Bintu et al., Spatial organization and detection of social odors in mouse primary olfactory system, Cell (2026), https://doi.org/10.1016/j.cell.2026.03.053

1) The 15 MERFISH preamplifiers and *Egr1* specific preamplifier were mixed together at a concentration of 30nM each in hybridization buffer (40% formamide, 10% dextran sulfate in 2xSSC) and hybridized to the sample for 30 minutes at 37 °C.
2) The sample was washed in 20% formamide in 2xSSC for 20 minutes at 37 °C.
3) The 15 MERFISH amplifiers and *Egr1* specific amplifier were mixed together at a concentration of 30nM each in hybridization buffer (40% formamide, 10% dextran sulfate in 2xSSC) and hybridized to the sample for 30 minutes at room temperature.
4) The sample was washed in 30% formamide in 2xSSC for 20 minutes at 37 °C.

Then to readout the MERFISH signal across combinations of OR transcripts, fluorescent readout probes were sequentially added to the sample using a fluidics device connected to an inverted epifluorescence microscope as described in Su et al.[69] An identical labelling and imaging procedure was used for both the MOE and the OB.

MERFISH decoding of OR identity of sensory neurons in the MOE

The OR identity and volume occupied by each sensory neuron labelled was determined by first defining the best correlated groups of 3D pixels across each combination of 4 out of the set of 15 readout images corresponding to each MERFISH bit. These groups of pixels were determined by scanning ~2.5 μm cubes across the epithelium and calculating all the Pearson correlation coefficients between the fluorescent signal across all the pairs of readout images.

For these groups of pixels with high correlation (>0.6) we further applied a density-based clustering algorithm to group pixels corresponding to the same neuron and separate out distinct neurons. For this final filtered group of pixels, matching a particular set of 4 images, we found the OR identity based on the corresponding set of 4 readouts designed for the probes against the OR transcripts.

Imaging and aligning the OB sections

6 OB coronal sections were processed in each imaging experiment. Two pools of MERFISH probes (one targeting 500 ORs and the other targeting the remaining 600 ORs) were hybridized in an alternating manner across the sections.

To reduce imaging time, first a low magnification objective (10X) was used to image the nuclear signal (DAPI) across entire OB sections. This low-resolution overview of the sections allowed the high magnification (40X) MERFISH imaging to focus and tile only the glomeruli layer.

Approximately 160 coronal sections were imaged per animal, covering the bilateral OBs of 2 CD1 female mice (11 week) (Charles River) approximately uniformly in 16-18 μm increments. Each of the sections were aligned and corrected for sectioning distortions using the nuclear signal. First small subimages (of ~ 100 μm in size) covering the glomeruli layer were individually rigidly aligned across adjacent sections by maximizing the correlation upon varying the angle and translation parameters. These served as matching features across the sections to be aligned. Using the consensus angle and translation, the adjacent slices were rigidly aligned. The remaining misalignment was corrected by gaussian interpolating the residual displacement of the matching features. Briefly for each point on the section, the additional distortion was calculated and corrected for from the residual displacement of the neighboring matching features which were weighed in using a gaussian term with a standard deviation ~75 μm (similar to the glomeruli size). A custom graphics user interface was designed in Python and used to manually correct or exclude any features that were not correctly assigned via the automated procedure. By successively aligning each of the neighboring sections a 3D volume of the bulb can be reconstructed from the stack of ~160 sections.

MERFISH decoding of OR identity of glomeruli in the OB

Glomeruli segmentation

The glomeruli within the glomerular layer of each coronal section of the olfactory bulb were segmented using Cellpose,[49] a convolutional neural network-based algorithm designed primarily to segment cells/nuclei. This model was found, in general, to segment well roughly circular objects other than cells and nuclei. Briefly, the nuclear fluorescent signal (stained with DAPI) of the cells within the OB sections was inverted and rescaled to meet the dimension specifications of the pretrain Cellpose model. The nuclear pretrained model was used with low cutoff probability for the segmentation to ensure that the entire glomeruli layer is partitioned into glomeruli.

MERFISH staining into the olfactory bulb

Multiplexing was performed at a scale of 500-600 genes per section across two orthogonal sets of ORs. Glomeruli are typically 70-100 μm in size and cover a few successive sections. Therefore, by alternating between the two successive sets of probes used for hybridization across the serial sections, each glomerulus was interrogated across the entire 1,100 receptor repertoire.

Glomeruli decoding

Across the glomeruli layer, individual transcripts were identified using an algorithm for co-localizing 3D local maxima.[69] Briefly, after localizing single molecules in 3D in each MERFISH readout image, we filter only the molecules co-localizing within ~160 nm (across the x,y and z axes) in at least 4 out of 15 MERFISH readout images. For the molecules that colocalize across more than 4 MERFISH readout images we consider only the brightest 4. For each of these filtered molecules their OR identity is determined by matching their combination of 4 colocalizing MERFISH readouts to the unique combination of 4 readouts assigned during the MERFISH probe design for each OR gene. A brightness threshold is determined for each experiment to best separate the brightnesses of molecules mapping to the 500-600 ORs targeted vs the ORs not targeted during that experiment. This brightness threshold was applied to filter out the dim molecules contributing to noise.

Please cite this article in press as: Bintu et al., Spatial organization and detection of social odors in mouse primary olfactory system, Cell (2026), https://doi.org/10.1016/j.cell.2026.03.053

For each segmented glomerulus we counted the number of transcripts of each OR and assigned it the identity of the most enriched OR if the number of identified transcripts was higher than 10 and the enrichment of the number of transcripts within the glomerulus was higher than 10 times over the other glomeruli within the section. The glomeruli identified in each section were mapped into the 3D volume of the OB reconstructed as described in the section above.

A few expected projections were not identified (i.e. projections of Olfr15 not detected in one of the bulbs). Overall, projections for ~60% OR genes across the imaged OBs were first identified in this way. A potential source affecting the detection efficiency of OR glomerulus identity is the uneven distribution of the number of OR transcripts present in each glomerulus. Indeed, while for certain glomeruli we could reliably identify >50 OR transcripts per glomerular structure (Figures 3B and 3C), for other OR genes the corresponding glomeruli had less than 10 OR transcripts in each 2D coronal section, which was is below the limit of reliable detection. To increase the coverage we relaxed the identification criteria to more than 5 molecules instead of 10 if the same OR identity glomerulus was consistently identified within a similar position (within 500 μm) across multiple OBs.

Gene expression imputation in the MOE and OB

Single-cell sequencing data from cells isolated from the MOE of six C57BL/6J animals[44] were used for calculating gene expression imputations in the MOE and OB. The previously published annotation[44] was employed to exclude non-OSN cells and classify OSNs. For each OR/TAAR gene, the expression levels of each gene were averaged across their corresponding OSN populations. The average gene expression values for each OSN type were then spatially transferred to individual OSN positions identified by MERFISH across reference MOE slices. Subsequently, spatially transferred gene expressions were averaged at each point on the MOE surface, considering all OSNs located within a 50 μm radius. A similar strategy was employed for OB surface mapping, where OSN-type averaged gene expressions were assigned to each OSN glomerular projection. Expression values were again spatially averaged within a 400 μm radius around each OB surface point. Finally, gene expression imputation values were normalized by dividing by the 99th percentile of the signal across each surface. We note that these imputations are intended to allow the visualization of the correlations of differential transcription across OSN populations and their spatial location within the MOE or their projection into the OB.

Predicting glomerular positions based on gene expression and imputation

To determine if differential gene expression across OSNs is predictive of the location of their OB projection, we modified the gene expression imputation approach described above to remove the contribution of the OSN type being evaluated. Specifically, for each OSN type, gene expression imputations were recalculated by transferring and averaging gene expression data from all other OSN types, excluding the selected OSN type. We then computed Pearson correlation coefficients between these modified imputations across the OB surface and the average gene expression profile of the selected OSN type. Positions exhibiting the highest correlations within both the medial and lateral regions of the OB reference surface were identified as predicted projection locations based on gene expression.

Olfactory cue exposures

Adult (8-11 week) C57BL/6J (Jackson Laboratories) or CD1 mice (Charles River), including both females and males, were used in this study. Prior to exposures, all animals except mothers, were single housed for 2-7 days prior. CD1 mothers (2-5 days post birth) were single-housed into the same cage for 24h upon removing their pups from the home-cage. The cue was introduced in the home-cage of the animal to stimulate investigation of the foreign cue and minimize the introduction of other cues. After 30 minutes of exposure, in which the subject mice were allowed to freely interact, the animals were sacrificed. Then the MOE/OB was dissected (within 5-10 minutes) and freshly embedded in OCT (Tissue-Tek) and frozen in dry ice. The MOE was placed in an Eppendorf tube in PBS and degassed for 1 minute to remove air.

Acetophenone exposure

Following an odor exposure procedure published previously,[30] we spotted 10μL of undiluted acetophenone solution onto a piece of absorbing paper encased into a cassette and introduced it into the cage housing an 8-week C57BL/6J male. As in Jiang et al.,[30] we used 2 distinct concentrations of acetophenone in the spotted solution: undiluted 100% acetophenone and 1% acetophenone (diluted in DMSO), following the protocol in Jiang et al.[30]

Cat bedding exposure

~50 mL of soiled bedding was freshly sampled from the litter box of an adult female cat and introduced into the cage of the mouse (8-week C57BL/6J male) as described above. Bedding material was used expecting to contain a naturalistic mixture of olfactory odors excreted from the animal, including urine, feces, saliva, and fur.

Social cue exposure

A single C57BL/6J male or female mouse (8-11 weeks), or 4-5 pups (age postnatal day 2-5) were introduced into the home-cage of a CD1 mouse (male or female, 8 weeks). The animals were allowed to freely interact for 30 minutes after which the CD1 subject mice were sacrificed and their MOEs harvested as described above.

QUANTIFICATION AND STATISTICAL ANALYSIS

Correlation analysis

To asses the degree of correlation between different measures we reported the Pearson Correlation Coefficient (ρ) calculated using the *corcoef* function in the *numpy* package in *Python* for: Figures 1F, 1G, 2F, 2G, 3H, 3L, 3N, 5E–5G, S2C–S2G, S3F, and S4G–S4I.

Please cite this article in press as: Bintu et al., Spatial organization and detection of social odors in mouse primary olfactory system, Cell (2026), https://doi.org/10.1016/j.cell.2026.03.053

Statistical tests

Wilcoxon two-sided ranksums statistical test (*ranksums* function in *scipy.stats* package in *Python*) were used to asses statical significant changes between quantities in: Figures 5H, 6D, 6E, 6I, and S6H. Corresponding *p* values and numbers are indicated in figure legends or associated main text. Wilcoxen test was preferred as it does not assume a normal distribution for the underlying quantifications.

p values were calculated upon uniformly sampling the OR distribution for Figures 2K, S2, S2N, and S2O (* denotes $p < 0.05$).

Fisher exact two-sided test was used using *fisher_exact* function in *scipy.stats* package in *Python* for Figure 6A. Number of animals per condition is indicated in the figure legend. The *p* values are tabulated in Table S7. Fisher exact test was used to handle the limited number of positive OSNs detected for each exposure condition.

Box plots centers mark medians and span 25th/75th percentiles; notches denote 95% confidence intervals; whiskers mark the 15th/85th percentiles unless otherwise stated in the figure legends.

Estimating the relative contributions of genomic distance and sequence similarity of ORs to the spatial overlap of their OSNs

In an attempt to disambiguate the relative contributions of genomic distance and sequence similarity of ORs to the spatial overlap of their OSNs, we z-scored the spatial overlap (S), the genomic distance (G) and the phylogenetic sequence similarity (P) across all OR gene pairs and fitted a multivariate linear regression model: $S = A\,G + B\,P + \varepsilon$ where A and B are the coefficients marking the contribution of genomic distance and sequence similarity respectively and ε is a noise term. We analyzed 145,568 OR gene pairs and found that A = -0.125 and C=-0.151 with corresponding t-statistics -41 and -50 respectively. We note the negative sign of the coefficients indicates higher spatial overlap for either ORs closer in sequence or on the genome. We noticed similar contributions to the spatial overlap from both sequence similarity and genomic distance with a bias towards sequence similarity being more predictive than genomic distance.

Supplemental figures

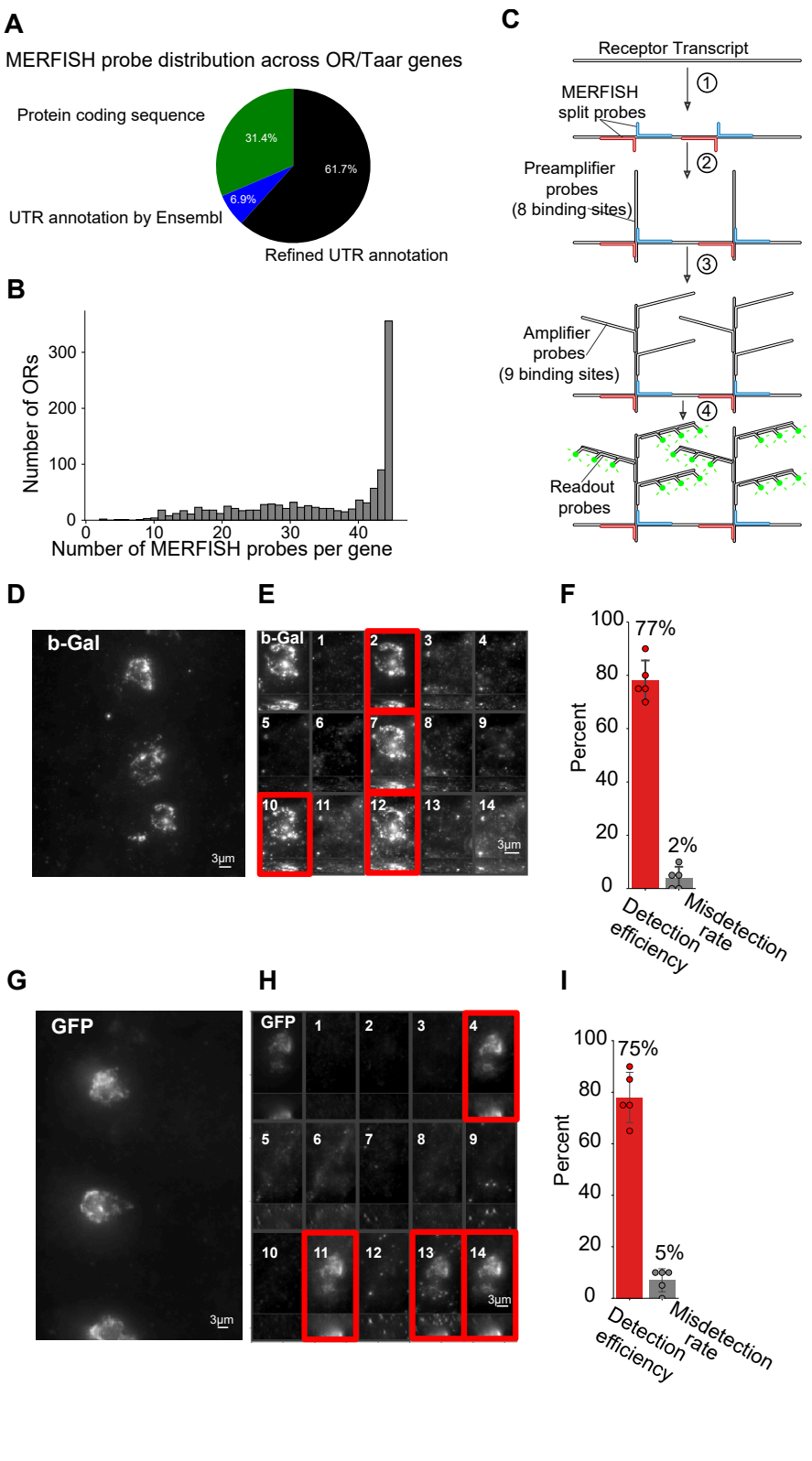

(legend on next page)

Figure S1. MERFISH probe design for ORs/TAARs and validation of OSN type identification with transgenic reporter lines, related to Figure 1

(A) Pie chart with the percentage of MERFISH encoding probes targeting the receptor coding region (green), the Ensemble-annotated UTR regions (blue), and the extended UTR annotations[40] (black).

(B) Histogram with the number of split-pairs of encoding probes across the OR/Taar repertoire.

(C) Schematic of the split-branched amplification scheme. (1) Hybridization of split-pair MERFISH encoding probes to receptor RNA. (2) Preamplifier probes (200-nt) bind to colocalized split-pair encoding probes. (3) Amplifier probes (200-nt) bind to the 8 repetitive 20-nt binding sites on the preamplifiers. (4) Fluorescent readout probes (30-nt) bind the repetitive 20-nt binding sites on the amplifiers.

(D) smFISH signal for β-gal in a coronal MOE section from an *Olfr17-IRES-tau-lacZ* transgenic animal.

(E) Max-intensity projection of a β-gal+ neuron showing β-gal smFISH signal (top left panel) and MERFISH signal across 14 readout cycles. Higher signal in cycles 2, 7, 10, and 12 (red) identifies the cell as *Olfr17*+.

(F) Detection efficiency (fraction of β-gal+ cells identified as *Olfr17*+ in MERFISH) and misdetection rate (fraction of *Olfr17*+ cells in MERFISH which are β-gal−) across two sections. The mean and standard deviation are plotted.

(G–I) Same as (D)–(F), respectively, but for *Olfr16* in an *Olfr16-IRES-tau-GFP* transgenic line.

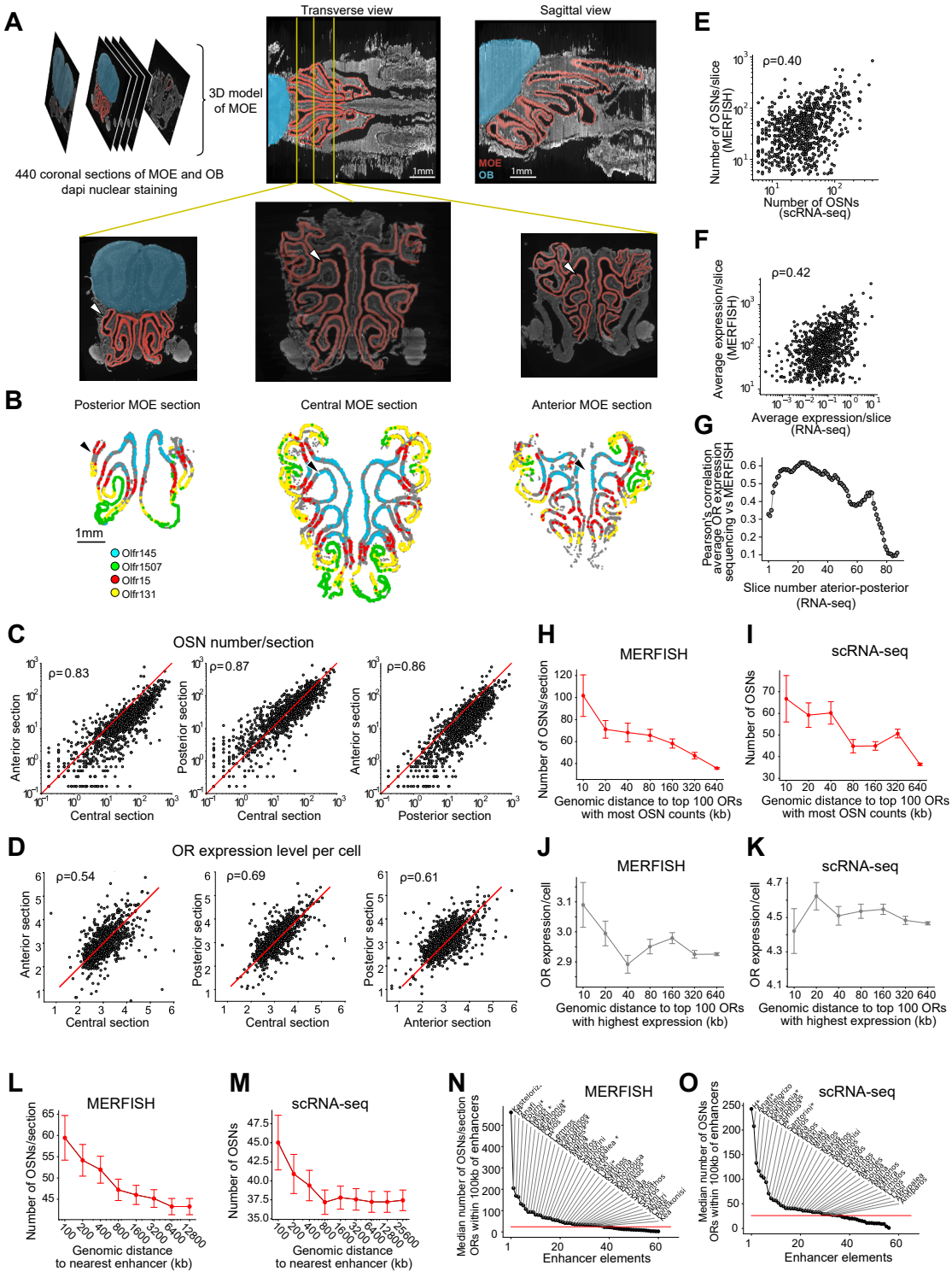

Figure S2. Validating imaging-based OSN quantifications using sequencing-based results, related to Figure 1

(A) Serial coronal sectioning of the MOE and DAPI staining enabled a 3D reconstruction of the entire MOE and the identification of the sections used for MERFISH.

(B) Representative coronal sections from the most posterior, central, and anterior MOE sampled by MERFISH, overlayed with OSN positions of 4 example ORs. Arrows indicate the turbinate features used to locate the slices within the 3D MOE volume in (A).

(C and D) Correlations between the number of OSNs per section (C) and the per-OSN expression level (D) for each OR comparing anterior with central, posterior with central, and anterior with posterior sampled MOE sections.

(legend continued on next page)

(E) Correlation between the average number of OSNs per section quantified by MERFISH and the number of OSNs quantified by snRNA-seq[44] across ORs. Pearson's correlation coefficient indicated.
(F) The average OR expression per MOE slice quantified by MERFISH and bulk RNA-seq.[17]
(G) Plot of the Pearson's correlation coefficients of OR expression per slice quantified by MERFISH and by bulk RNA-seq along ~85 coronal sections covering the entire MOE.[17]
(H) Correlation between the average number of OSNs per section quantified by MERFISH and the genomic distance from the top 100 most frequent OR types.
(I) Same as (H) using OSN numbers quantified by snRNA-seq.[44]
(J) Correlation between the per-OSN OR expression quantified by MERFISH and the genomic distance from the top 100 ORs with the highest expression.
(K) Same as (J) using OR expression per OSN numbers quantified by snRNA-seq. Error bars mark the standard error of the mean.
(L) Correlation between the number of OSNs per section quantified by MERFISH and the genomic distance from the nearest annotated enhancer element.
(M) Same as (L) using OSN numbers quantified by snRNA-seq.
(N) Plot of median number of OSNs/section (based on MERFISH) for the ORs within 100 kb of each enhancer element. Red line indicates the median OSN counts across all ORs.
(O) Same as (N) for OSN numbers quantified based on the scRNA-seq.

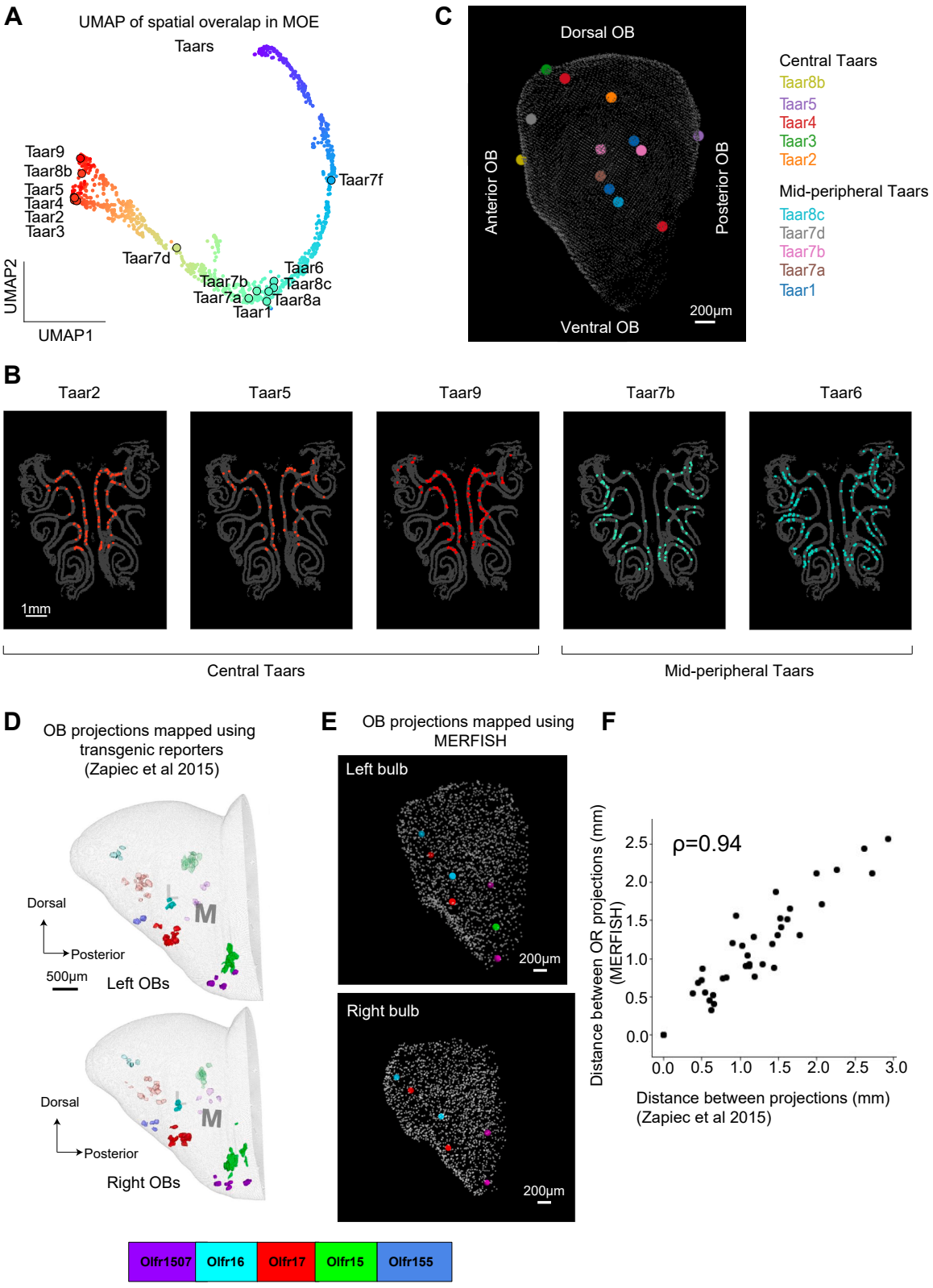

(legend on next page)

Figure S3. The spatial distribution of TAARs and validation of OB projection, related to Figure 2

(A) UMAP embedding of ORs based on their spatial overlap (reproduced from Figure 2B) with TAAR genes overlayed. TAARs are primarily located in the central or mid-peripheral MOE.

(B) Example images of the spatial distribution of 3 TAAR genes within the central MOE and 2 TAAR genes within the mid-peripheral MOE.

(C) Image highlighting the TAAR projections detected within the OB.

(D) 3D projections for 5 ORs identified by serial two-photon tomography in transgenic lines with fluorescently labeled ORs. The left and right bulbs of multiple animals were aligned to construct a unified map. This panel is reproduced from Zapiec and Mombaerts.[18]

(E) MERFISH-identified projections for the corresponding ORs across the left and right OB of a female mouse.

(F) Correlation between the pairwise distances of OR projections identified in transgenic reporter lines and the corresponding pairwise distances of OR projections identified by MERFISH (Pearson correlation coefficient of 0.94).

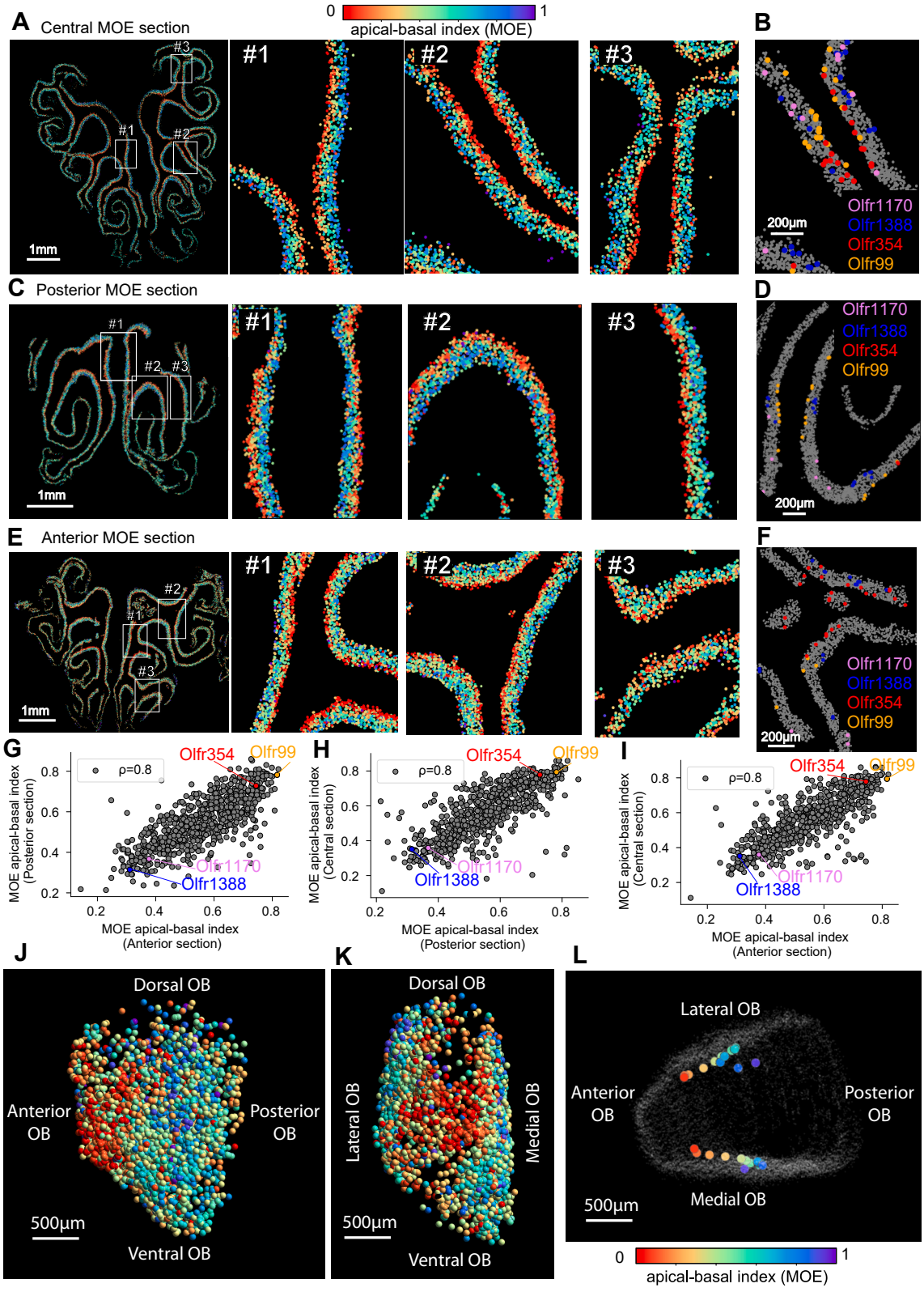

(legend on next page)

Figure S4. The apical-basal position of OSNs in the MOE correlates with the A-P position of their projections in the OB, related to Figure 3

(A) Example image of a central MOE section with OSNs labeled based on the average apical-basal position of each OR type. Zoom-ins are shown for 3 different MOE regions.

(B) Zoom-in image on a MOE region with the positions of 4 example OSN types highlighted (*Olfr354* and *Olfr99* are more apical, while *Olfr1388* and *Olfr1170* are more basal).

(C–F) Same as (A) and (B) for a posterior section (C and D) and an anterior MOE section (E and F), respectively.

(G–I) Pairwise correlation of the apical-basal position of OSNs between the most anterior, posterior, and central sections sampled in the MOE.

(J) OB projections colored based on the apical-basal position of their corresponding OSNs in the MOE (medial side).

(K) Same as (J) shown from a different view angle of the OB.

(L) Image of the OB together with the average positions of OR projections binned based on the apical-basal positions of the corresponding OSNs in the MOE. Two parallel axes (one for medial projections and one for lateral projections) emerged along the A-P axis of the OB.

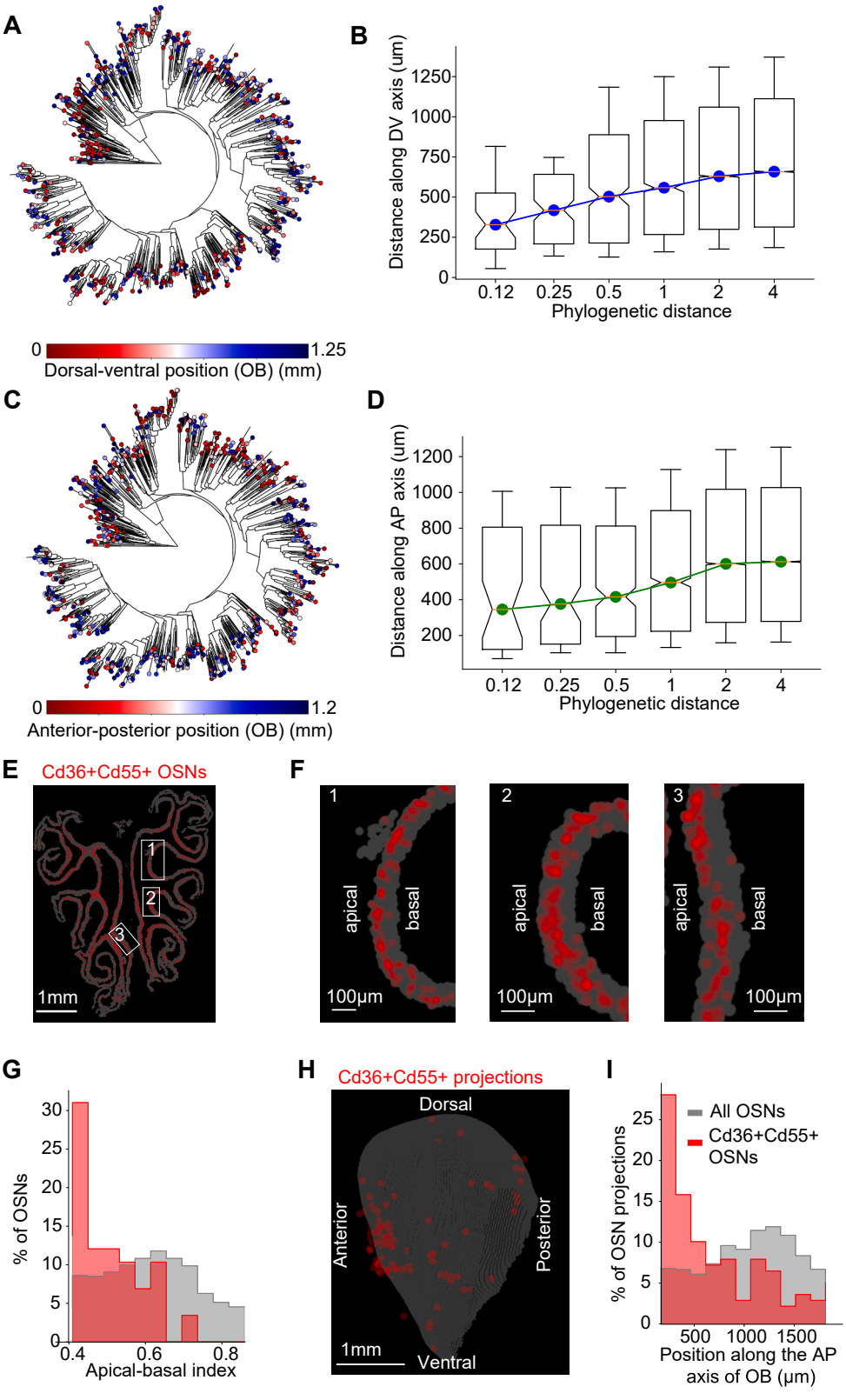

(legend on next page)

Figure S5. D-V and A-P bias of OB projections, related to Figure 4

(A) Phylogenetic tree connecting *ORs* based on their sequence similarity, constructed as in von der Weid et al.[31] Each node, representing an OR, is colored based on the D-V position of the OB projection as indicated in the colormap.

(B) Correlation between distances of *ORs* along the phylogenetic tree of pairs of ORs and distances along the D-V projection axis. For each pair of ORs, we calculated their distance along the tree in (A) and then binned these distances. For each bin, we represent a box plot marking the median D-V distances between the ORs within the corresponding phylogenetic distance range. Notches represent 95% confidence intervals, the boxes mark the first and third quartiles, and the whiskers mark the 15th and 85th percentiles.

(C and D) Same as (A) and (B), respectively, for the A-P axis of the OB.

(E) The spatial distribution in a central MOE coronal section of *Cd36*+ and *Cd55*+ OSN types based on snRNA-seq.

(F) Zoom-in images of the coronal section in (E) as indicated by the boxed regions 1,2,3.

(G) Histograms with the apical-basal index of the OSN types that are *Cd36*+ and *Cd55*+.

(H) MERFISH image of the OB onto which the projections corresponding to *Cd36*+ and *Cd55*+ OSNs are highlighted in red. Gray marks the surface of the OB.

(I) Histograms with the A-P position of the OB projections of *Cd36*+ and *Cd55*+ OSNs.

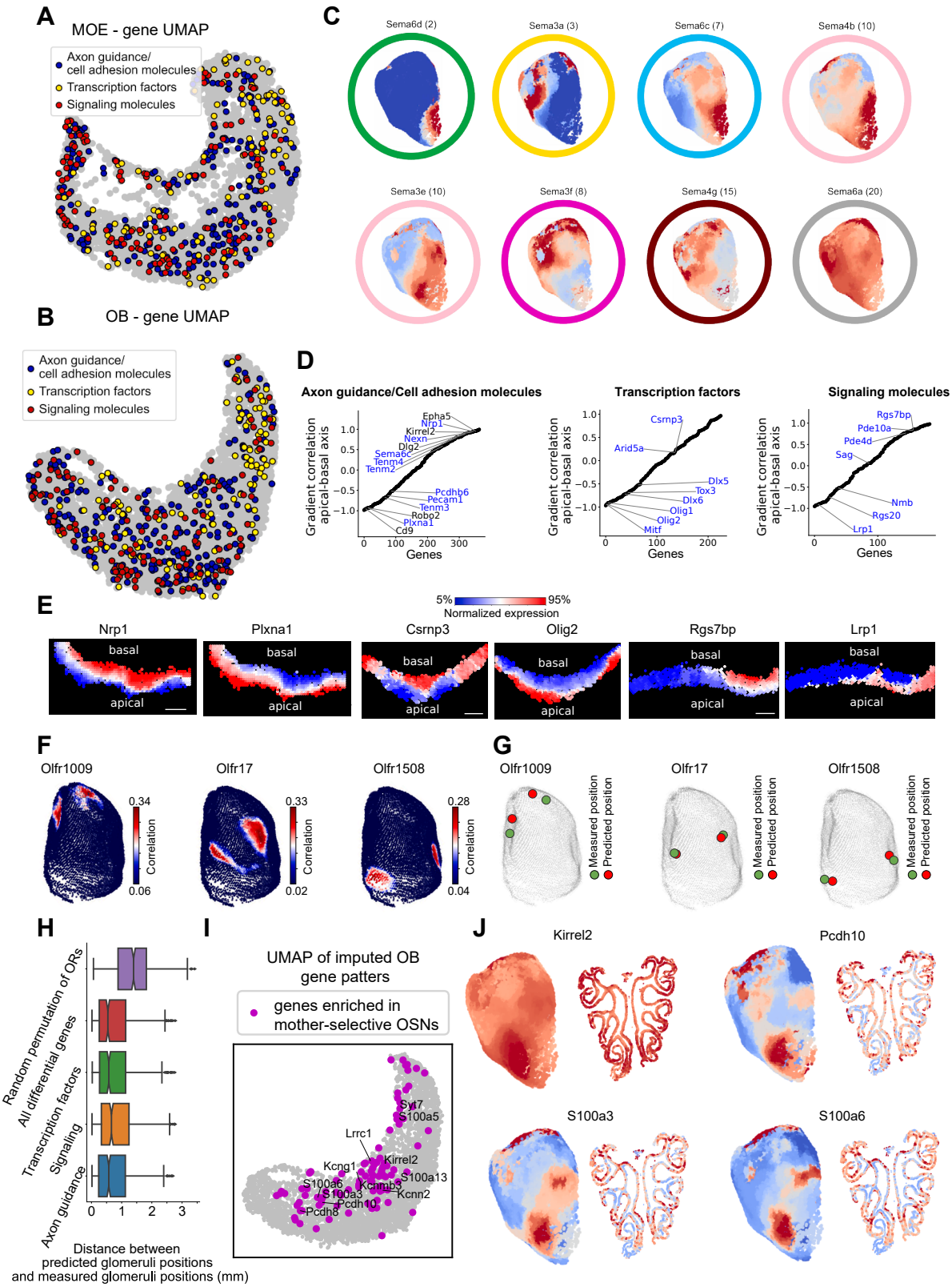

(legend on next page)

Figure S6. The expression patterns imputed within MOE or OB for specific classes of genes, related to Figure 4

(A) UMAP representation of the MOE imputed spatial patterns (reproduced from Figure 4D) with the axonal guidance/cell adhesion molecules, transcription factors, and signaling molecules overlayed.

(B) Same as (A) for the OB UMAP reproduced from Figure 4F.

(C) The imputed spatial patterns of the semaphorin gene family in the OB.

(D) Plot of Pearson's correlations across genes between imputed MOE expression and a linear gradient along the basal-apical axis of the MOE. Left, middle, and right panels catalog basal-apical expression across axonal guidance/cell adhesion molecules, transcription factors, and signaling molecules, respectively. The gene names marked in blue are the ones highlighted in Figure 4 to facilitate comparison. Black gene names are additional genes with an absolute correlation >0.75 and a fold change larger than 50% between apical and basal expression.

(E) Example imputed gene expression plots within turbinates of the MOE. Scale bars, 100 μm.

(F) Correlations between the average gene expression of *Olfr1009*, *Olfr17*, and *Olfr1508* OSNs and the imputed expression across the OB from all the other OSN types. The correlations were computed across the top ~5,000 differentially expressed genes across the glomerular layer.

(G) OB image showing the projections for *Olfr1009*, *Olfr17*, and *Olfr1508* identified by MERFISH (green) and the two inferred projections based on the maximum medial and lateral correlations in (F) (red).

(H) Box plots showing the distances between the computationally inferred glomeruli positions and the MERFISH-identified glomeruli positions across the OR repertoire when using different sets of genes for computing the correlation described in (A). Purple box plot shows the distances between the predicted inferred projections and the measured projections using the top 5,000 differentially expressed genes upon randomly shuffling the OR identities.

(I) UMAP embedding the imputed OB patterns, in which the genes enriched in mother-selective OSNs are highlighted in magenta. The names of a few representative genes are marked.

(J) Images of imputed OB and MOE patterns of 4 representative genes enriched in mother-selective OSNs.

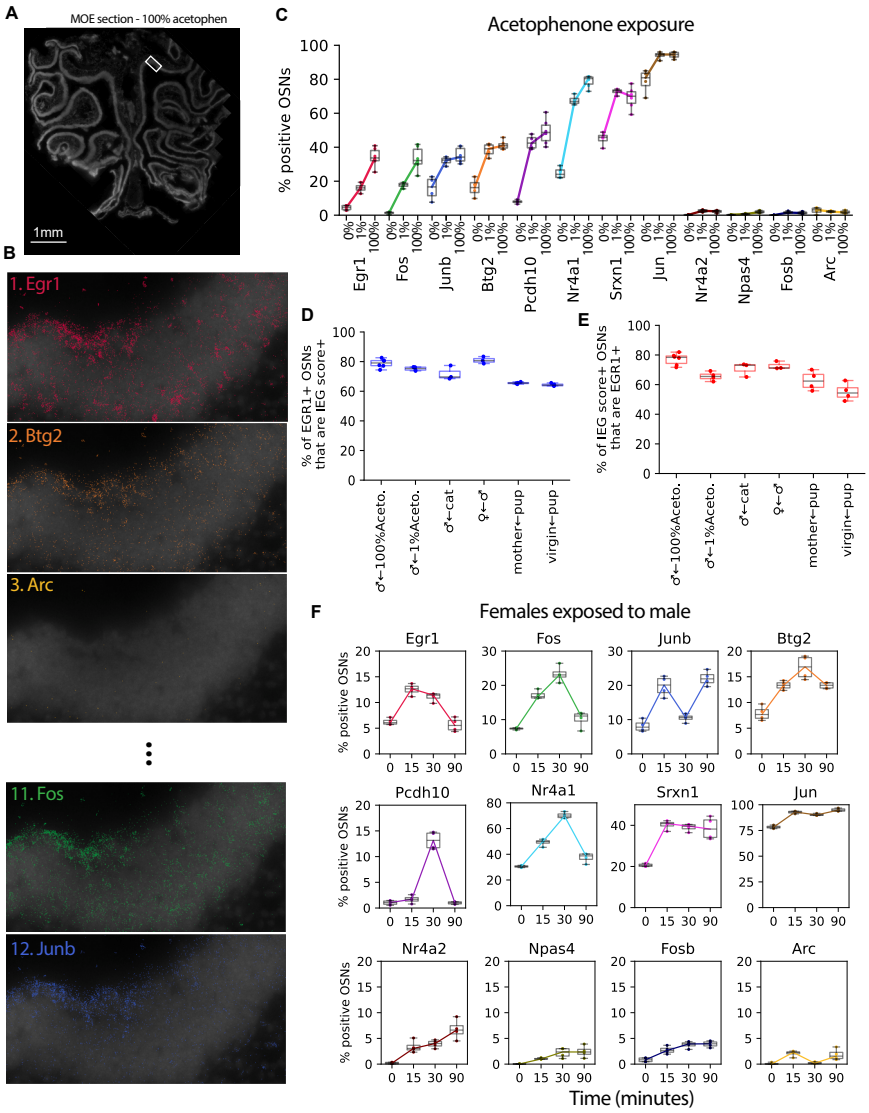

Figure S7. Immediate early gene expression in the MOE upon exposing animals to different olfactory cues, related to Figure 5

(A) Example central coronal section of MOE exposed to 100% acetophenone.

(B) Zoom-in images of single-molecule FISH signal of mRNA, for example, IEGs imaged in response upon 100% acetophenone exposure.

(C) Box plots with the percentage of positive OSNs (with more than 5 mRNA of each IEG) in response to 0% (unstimulated animals), 1%, and 100% acetophenone.

(D) Box plot of the percentage of OSNs positive for *Egr1* (>5 molecules per cell) and OSNs positive based on an IEG score calculated as the average *z*-scored expression of six genes: *Egr1*, *Fos*, *Junb*, *Btg2*, *Pch10*, and *Nr4a1*. Six olfactory stimulation conditions are quantified, as indicated, across multiple sections each.

(E) Box plot of the percentage of positive OSNs based on the IEG score that are also positive for Egr1. IEG score is calculated as in (A).

(F) Box plots of percentage of positive OSNs (>5 molecules per cell) for 12 candidate IEGs across female animals exposed to males for the unstimulated condition, and upon 15, 30, and 90 min.